Multiscale Moving Boundary Modelling of Cancer Interactions with a Fusogenic Oncolytic Virus

Alzahrani, Talal; Eftimie, Raluca; Trucu, Dumitru

Published in:
Mathematical Biosciences

DOI:
10.1016/j.mbs.2019.108296

Publication date:
2020

Document Version
Peer reviewed version

Multiscale Moving Boundary Modelling of Cancer Interactions with a Fusogenic Oncolytic Virus: the Impact of Syncytia Dynamics

Talal Alzahrani, Raluca Eftimie, Dumitru Trucu*

Division of Mathematics, University of Dundee, Dundee, DD1 4HN

Abstract

Oncolytic viral therapies is one of the new promising strategies against cancer, due to the ability of oncolytic viruses to specifically replicate inside cancer cells and kill them. There is increasing evidence that a sub-class of viruses that contain fusion proteins (triggering the formation of syncytia) can lead to better oncolytic results. Since the details of the tumour dynamics following syncytia formation are not fully understood, in this study we consider a modelling and computational approach to describe the effect of a fusogenic oncolytic virus on the multiscale dynamics of a spreading tumour. We show that for the baseline parameter values considered here, small syncytia diffusion coefficient leads to tumour reduction. Further tumour reduction can be obtained when we increase the probability of syncytia formation, in the context of different viral burst rates and death rates for individually-infected tumour cells and syncytia structures. Finally, we show that the type of syncytia diffusion coefficient (i.e., constant or density dependent) also impacts the outcome of the oncolytic viral therapy.

Keywords: multiscale cancer modelling, tumour–oncolytic virus interactions, syncytia formation

1. Introduction

Oncolytic viral therapy has become a promising anti-cancer treatment approach due to the ability of these viruses to preferentially replicate inside cancer cells and eliminate them [1]. While there are some clinical successes [2], there are still significant challenges that impede a wider and more common use of this type of therapy: from challenges associated with the systemic delivery of the viruses (and their elimination by various immune responses), to the physical barriers caused by the extracellular matrix (ECM) [3]. Regarding the systemic delivery of oncolytic viruses, the intravenous administration would be the preferable option, since viruses could thus reach both the primary tumours and the metastases. However, due to the immune system and other physiological filters which eliminate these viruses, the current approaches focus mostly on intra-tumoural injection of the oncolytic viruses [4]. Regarding the challenge caused by the physical barriers, namely the high interstitial fluid pressure and the physical presence of ECM, this can be tackled with the help of matrix-degrading enzymes that degrade various types of fibrillar matrix deposits and make space between cells, which might eventually increase the possibility of oncolytic viral infection [3].

While there are many types of oncolytic viruses used in experiments and in clinical trials [5, 6, 7], some lead to better anti-tumour results than others. For example, there is increasing evidence suggesting that a sub-class of oncolytic viruses which encode for fusion proteins (and thus lead to the formation of syncytia structures; see also Fig. 1) might lead to better anti-tumour effects compared to the non-fusogenic viruses [7, 8]. During infection with fusogenic viruses, viral fusion proteins that are used by these viruses to enter the cells, are transported to the surface of the infected cell where they mediate the fusion of this cell to the neighbouring uninfected cells [7, 8]. The syncytia structures are motile, as they extend large pseudopods to move (and their average instantaneous velocity could be slightly larger than the velocity of single cells [9]). This movement, together with the movement of single cells, was shown to play a role in the recruitment of more cells in the syncytia [9]. While these syncytia seem to contribute to the faster spread of the oncolytic virus through the unin-

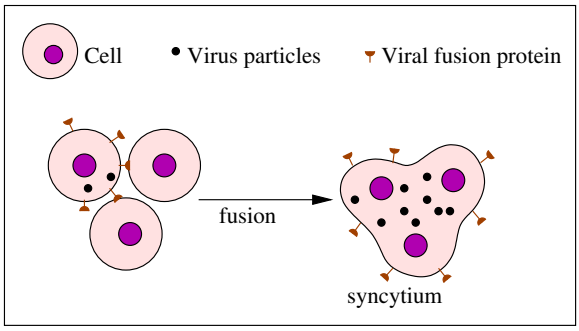

Figure 1: Graphical description of a viral-induced syncytium.

*Corresponding author
Email address: trucu@maths.dundee.ac.uk (Dumitru Trucu)

fected tumour via their higher viral yield and faster replication kinetics [8, 7, 10], the structures are usually viable for a short time (usually 2 days [11]) before they undergo immunogenic cell death. We should also mention here that there are still many unknown aspects surrounding the role of syncytium formation on the spread of an infection, such as whether this syncytium could also "sink" an infection [12].

Therefore, to further enhance the therapeutic potential of the fusogenic viruses, one needs to understand better the interactions between these motile structures and the multiscale aspects of cancer invasion (e.g., the movement of cancer cells versus the movement of syncytia, the degradation of ECM by cancer cells and its impact on the formation and spread of syncytia). Mathematical models can test and propose new hypotheses regarding these multiscale interactions.

The majority of the mathematical models that focus on fusogenic oncolytic viruses consider only the implicit (temporal) dynamics of syncytia cancer cells [13, 14, 15]. There are also a few mathematical models that consider the explicit dynamics of the syncytia; see for example [16] for a temporal (ODE) model, and [17, 18] for spatio-temporal models. Moreover, the large majority of these models focus on a single-scale dynamics of viruses spread among cancer cells. Nevertheless, there are also a very few multiscale models for oncolytic virus infections [19, 20].

In this study we revisit the novel multi-scale mathematical modelling framework introduced in [20] for cancer cells interactions with oncolytic viruses, and extend it to incorporate also the dynamics of the syncytia generated by fusogenic viruses. At the macroscopic scale, we investigate the dynamical interactions between three types of cancer cells (uninfected, viral-infected and syncytia-forming cells) and oncolytic viruses, in parallel with their movement through the extracellular matrix (ECM). At the microscopic scale, we focus on the proteolytic dynamics of the urokinase plasminogen activator system (uPA) that locates at the invasive edge of the tumour site and is responsible for the degradation of the ECM. The macro-scale (tissue-scale) dynamics connects with the micro-scale (cell-scale) dynamics through a double feedback link that will be explained in more detail in the next section.

Using this new multiscale moving-boundary mathematical model, we investigate numerically a few hypotheses regarding syncytia movement: via pure diffusion (faster/slower than the diffusion of single infected cancer cells), or via diffusion combined with haptotactic movement towards ECM components. We also investigate the effect of density-dependent diffusion coefficient for the syncytium structure (since it is unknown whether there is any relationship between the speed of syncytium and the density of virus particles that created it, and/or the density of ECM that acts as a barrier for virus/cells movement). Finally, we investigate the impact of different probabilities of syncytium formation on the outcome of oncolytic therapy.

2. Modelling Hypotheses and Setting

In this study, we focus on the naturally multiscale nature of the cancer-virus interaction, and explore key parts of this process (which includes for the first time also the formation of virus-induced syncytia structures) through the two-scale modelling platform introduced in [21]. Specifically, while the direct interaction between the cancer cell population and the virus (which can lead to the formation of syncytia depicted in Figure 1) is observed at macroscale, this has implications within cell-scale matrix-degarding enzymes proteolytic dynamics that takes place along the invasive edge of the tumour. As this micro-dynamics is linked to the macroscale through a non-local double feedback link (see Figure 2), this crucially determines the changes in spatial tumour morphology during its evolution.

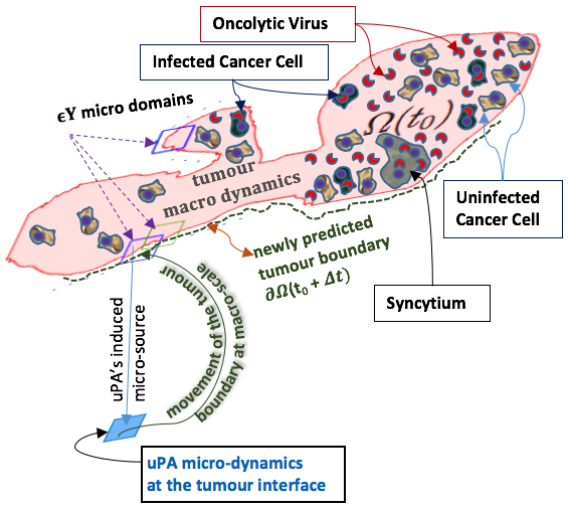

Figure 2: Schematics of the multiscale moving boundary approach.

2.1. Macroscopic Model for Virus-Tumour Interactions via Syncytium Formation

Starting with the multi-scale moving boundary mathematical framework concepts introduced in [21, 22] and the syncytium assumptions introduced in [16], we describe a new multi-scale spatio-temporal mathematical model for the interactions between cancer cells and a fusogenic oncolytic virus (which leads to the formation of syncytia structures). Maintaining here the terminology of the multiscale framework introduced in [21], we denote the tissue-scale (macro-scale) growing solid tumour by $\Omega(t)$ and we assume that this evolves within a maximal cube of tissue $Y \in \mathbb{R}^N$, $N = 2, 3$, and so $\Omega(t) \subset Y$, $\forall t > 0$. As illustrated in Figure 2, at the macroscopic-scale, we focus on the dynamic interactions between spatially distributed uninfected cancer cells $c(x, \cdot)$, infected cancer cells $i(x, \cdot)$ and syncytia cancer cells $s(x, \cdot)$ with the oncolytic virus (OV) particles $v(x, \cdot)$, while taking into account the surrounding extracellular matrix (ECM) density $u(x, \cdot)$, $\forall x \in \Omega(\cdot)$.

(The dynamics occurring at the microscopic scale and its *top-down* and *bottom-up* links to the macroscale will be detailed in Section 2.2).

Before we describe the model equations, let us denote by T the total cancer cells density, which is composed of uninfected (c), viral-infected (i) and syncytia (s) cells, i.e. $T = c + i + s$. The total density of viral-infected cells is denoted by $i_{tot} = i + s$.

Following biological evidence from several experimental studies [23, 24, 25, 26], we assume that the uninfected cancer cells exhibit both random and directed movements. The random movement is represented here via a diffusion process (see [27]). The cell directed movement that we address here is the one towards ECM gradients, and so adopting a similar approach as in [28], this is explored here via a haptotactic process. At the same time, based on further biological evidence [29, 30, 31], we assume here that the cell proliferation process is govern by logistic growth. Finally, the cell population can decay due to infection caused by oncolytic viruses at a rate ρ and to fusion with neighbouring infected cancer cells i at a rate κ. Hence, all these considerations lead to the following governing equation for the cell uninfected population, namely:

$$\frac{\partial c}{\partial t} = D_c \Delta c - \eta_c \nabla \cdot (c \nabla u) + \mu_1 c(1 - c) - \rho c v - \kappa c i. \quad (1)$$

where $D_c > 0$ is a constant diffusion coefficient, $\eta_c >$ represents a constant haptotactic rate, μ_1 is the logistic proliferation rate.

For the viral-infected cancer cells, drawing upon the same biological consideration as for the uninfected cancer cells [23, 24, 25, 26], we assume that also this population move randomly with diffusion coefficient D_i and can move in a haptotactic manner towards higher ECM gradients with rate η_i. The proliferation of viral-infected cancer cells is the result of infection with the oncolytic virus at a rate ρ, as well as the failure to form a syncytium structure that leads to individual infected cells. We denote by p_0 the probability that a syncytium structure will fail to form following the interactions between uninfected and infected cancer cells ($p_0 \kappa c i$). Thus, $(1 - p_0)$ will denote the probability that a syncytium will form (and $(1-p_0)\kappa c i$ will describe the formation of syncytia structures). Finally, the infected cancer cells die at rate δ_i. These assumptions are described by the following equation:

$$\frac{\partial i}{\partial t} = D_i \Delta i - \eta_i \nabla \cdot (i \nabla u) + \rho c v + p_0 \kappa c i - \delta_i i \quad (2)$$

For syncytia dynamics, we consider three distinct assumptions, namely:

(a) no diffusion (so their dynamics is the result of the formation of syncytia structure as described above, combined with death at a rate δ_s):

$$\frac{\partial s}{\partial t} = (1 - p_0)\kappa c i - \delta_s s. \quad (3)$$

(b) diffusion (with coefficient D_s) without haptotactic movement towards the nearby ECM components:

$$\frac{\partial s}{\partial t} = D_s \Delta s + (1 - p_0)\kappa c i - \delta_s s. \quad (4)$$

(c) diffusion (with coefficient D_s) and haptotactic movement (at rate η_s) towards higher ECM gradients:

$$\frac{\partial s}{\partial t} = D_s \Delta s - \eta_s \nabla \cdot (s \nabla u) + (1 - p_0)\kappa c i - \delta_s s. \quad (5)$$

For the extracellular matrix (ECM) we assume that it does not migrate nor diffuse, but can be remodelled. To describe this remodelling process, we assume that ECM components grow logistically at rate μ_2 (while competing for space with the cancer cells: uninfected, infected and syncytia). In addition, ECM is degraded by all three type of cancer cells: by uninfected cells at rate α_c, by viral-infected cells at rate α_i, and by syncytia at rate α_s. Therefore the evolution of the density of ECM components is described by the following equation:

$$\frac{\partial u}{\partial t} = -u(\alpha_c c + \alpha_i i + \alpha_s s) + \mu_2 u(1 - u - c - i - s) \quad (6)$$

Finally, we assume that the oncolytic virus particles proliferate when they are released by the infected and syncytia cancer cells at rates b_i and b_s, respectively. These virus particles have the ability to diffuse at rate D_v, and to move haptotacticaly towards higher ECM gradients at rate η_v. Moreover, the free virus particles are eliminated (i.e., die) at a rate δ_v. Their numbers are also reduced when they infect at a rate ρ (and thus become trapped inside) the uninfected cancer cells. The previous assumptions are described mathematically by the following equation:

$$\frac{\partial v}{\partial t} = D_v \Delta v - \eta_v \nabla \cdot (v \nabla u) + b_i i + b_s s - \rho c v - \delta_v v. \quad (7)$$

The above equations describe the non-dimensional macroscopic scale dynamics in three different cases of gradual increasing complexity, which we summarise below as follows:

First case: syncytia cancer structures do not diffuse on the spatial domain, but they still have interactions with the ECM components whenever they meet on the micro spatial domain (i.e. they still play a central role on ECM remodelling and degradation). The full macroscopic model is given by:

$$\begin{cases} \frac{\partial c}{\partial t} = D_c \Delta c - \eta_c \nabla \cdot (c \nabla u) + \mu_1 c(1 - c) - \rho c v - \kappa c i, \\ \frac{\partial i}{\partial t} = D_i \Delta i - \eta_i \nabla \cdot (i \nabla u) + \rho c v + p_0 \kappa c i - \delta_i i, \\ \frac{\partial s}{\partial t} = (1 - p_0)\kappa c i - \delta_s s, \\ \frac{\partial u}{\partial t} = -u(\alpha_c c + \alpha_i i + \alpha_s s) + \mu_2 u(1 - u - c - i - s), \\ \frac{\partial v}{\partial t} = D_v \Delta v - \eta_v \nabla \cdot (v \nabla u) + b_i i + b_s s - \rho c v - \delta_v v. \end{cases} \quad (8)$$

Second case: syncytia cancer structures have diffusion abilities, but they do not interact haptotactically with the nearby ECM's components. The full macroscopic model is therefore given by:

$$\begin{cases} \frac{\partial c}{\partial t} = D_c\Delta c - \eta_c\nabla\cdot(c\nabla u) + \mu_1 c(1-c) - \rho cv - \kappa ci, \\ \frac{\partial i}{\partial t} = D_i\Delta i - \eta_i\nabla\cdot(i\nabla u) + \rho cv + p_0\kappa ci - \delta_i i, \\ \frac{\partial s}{\partial t} = D_s\Delta s + (1-p_0)\kappa ci - \delta_s s, \\ \frac{\partial u}{\partial t} = -u(\alpha_c c + \alpha_i i + \alpha_s s) + \mu_2 u(1-u-c-i-s), \\ \frac{\partial v}{\partial t} = D_v\Delta v - \eta_v\nabla\cdot(v\nabla u) + b_i i + b_s s - \rho cv - \delta_v v. \end{cases} \tag{9}$$

Third case: syncytia cancer structures diffuse randomly in the spatial domain and also move haptotactically towards higher ECM gradients. Thus the full macroscopic model is given by:

$$\begin{cases} \frac{\partial c}{\partial t} = D_c\Delta c - \eta_c\nabla\cdot(c\nabla u) + \mu_1 c(1-c) - \rho cv - \kappa ci, \\ \frac{\partial i}{\partial t} = D_i\Delta i - \eta_i\nabla\cdot(i\nabla u) + \rho cv + p_0\kappa ci - \delta_i i, \\ \frac{\partial s}{\partial t} = D_s\Delta s - \eta_s\nabla\cdot(s\nabla u) + (1-p_0)\kappa ci - \delta_s s, \\ \frac{\partial u}{\partial t} = -u(\alpha_c c + \alpha_i i + \alpha_s s) + \mu_2 u(1-u-c-i-s), \\ \frac{\partial v}{\partial t} = D_v\Delta v - \eta_v\nabla\cdot(v\nabla u) + b_i i + b_s s - \rho cv - \delta_v v. \end{cases} \tag{10}$$

Furthermore, each of these coupled dynamics are accompanied by initial conditions

$$c(x,0)=c_0(x), \quad i(x,0)=i_0(x), \quad s(x,0)=s_0(x), \quad x\in\Omega(0),$$
$$u(x,0)=c_0(x), \quad v(x,0)=i_0(x), \quad x\in Y,$$

which will be specified explicitly with particular forms for numerical simulations in Section 3.
Finally, since we do not assume any transport across the boundary of the activity domains, each of these coupled dynamics are accompanied by Neumann zero boundary conditions, namely:

$$\left.\frac{\partial c}{\partial n}\right|_{\partial\Omega(t)} = 0; \quad \left.\frac{\partial i}{\partial n}\right|_{\partial\Omega(t)} = 0; \quad \left.\frac{\partial s}{\partial n}\right|_{\partial\Omega(t)} = 0;$$
$$\left.\frac{\partial u}{\partial n}\right|_{\partial Y} = 0; \quad \left.\frac{\partial v}{\partial n}\right|_{\partial Y} = 0;$$

were n represents simply the normal direction across the interface of the corresponding activity domain.

2.2. The Microscopic Proteolytic Dynamics and its Double Feedback to Link to Macro-Scale

As established biologically [32, 33, 34], the cell-scale molecular dynamics of the matrix degrading enzymes at the tumour invasive edge plays a critical role within the cancer cells invasion process. Several important families of matrix degrading enzymes are collectively secreted by the cancer cells within the outer proliferating rim of the tumour exercise a spatial transport in a cell-scale neighbourhood of the the tumour interface and this way cause a degradation of the peritumoural ECM, leading to continuous morphological changes in the macro-scale tumour boundary and ultimately resulting in further progression of the cancer in the surrounding tissue. Among these proteolytic enzymes, alongside the notable contribution of the family of matrix metalloproteinases (MMPs), a pivotal role within cancer invasion is played by the urokinase plasminogen activator (uPA) system, which not only that decomposes the ECM but also has implications in activating some of the MMPs as well as interfering with the activity of cytokines and growth factors (see [35]).

In brief, the uPA enzymatic system includes the coupled dynamics of three main molecular species (see [36, 37]), namely: (1) the inactive urokinase plasminogen activator (uPA); (2) uPA inhibitor (PAI-1); and (3) plasmin. In order to become active, the inactive uPA needs first to bind to the uPA receptors (uPAR). Once activated, the active uPA can activate the plasmin molecules (which are freely available in ECM) turning these into plasmin. However, at the same time, the active uPA molecules can also become inactive if these are bound by inhibitor molecules PAI-1, leaving this way the dynamics of the uPA system. Mathematically, we denote here the spatio-temporal distribution for each of these molecular species in the uPA system as follows:

- $a(y,\tau)$ represents the urokinase plasminogen activator (uPA), without distinguishing here between its active and inactive forms;
- $p(y,\tau)$ stands for the inhibitor PAI-1; and
- $m(y,\tau)$ is the plasmin;

where $(y,\tau)\in\mathbf{B}_{\|\cdot\|_\infty}(\partial\Omega(t_0),\epsilon)$, with $\mathbf{B}_{\|\cdot\|_\infty}(\partial\Omega(t_0),\epsilon)$ representing a cell-scale neighbourhood of radius $\epsilon>0$ for the tumour interface $\partial\Omega(t_0)$.

To address the multiscale dynamics of the cancer invasion process while accounting for the important role of the cell-scale (micro-scale) dynamics of the uPA system at the invasive edge of the tumour, the authors in [22] have applied the two-scale moving boundary framework initially introduced in [21] to explore the impact the uPA has upon the changes in the tissue-scale (macro-scale) tumour morphology of the growing cancer. Therefore, since here we build upon these two previous works and expand these by accounting also for the presence of an oncolytic virus with syncytia formation at macro-scale, to describe the micro-dynamics and its non-local feedback links with the tumour macro-dynamics that, let us briefly revisit in the following the key notations of the framework introduced and discussed in [21, 22]. Thus, to capture the micro-scale dynamics occurring at the invasive edge of the tumour, following a series of topological considerations, as described in [21], a covering family $\mathcal{P}$ consisting of overlapping cubes $\mathcal{P}(t):=\{\epsilon Y\}_{\epsilon Y\in\mathcal{P}(t)}$ is constructed from a section of *halfway shifted small cubes of* an appropriately chosen dyadic decomposition of the maximal tissue macro-cube Y (where

the tumour $\Omega(t)$ invades) that cover the tumour interface $\partial\Omega(t)$, which, in brief, exhibits and is completely determined by the following properties:

- each ϵY, also referred to as a *micro-domain*, provides a cell-scale neighbourhood of $\epsilon Y \cap \partial\Omega(t)$ of microscale size $\epsilon > 0$ with the particular properties that the regions captured inside and outside of the boundary, namely $\epsilon Y \cap \Omega(t)$ and $\epsilon Y \setminus \Omega(t)$, have topologically connected interiors;

- the family $\mathcal{P}(t) := \{\epsilon Y\}_{\epsilon Y \in \mathcal{P}(t)}$ covers completely the boundary $\partial\Omega(t)$.

Thus, at any given time $t_0 > 0$, the covering bundle $\mathcal{P}(t_0)$ enables the exploration of the uPA system dynamics on the cell-scale neighbourhood $\mathbf{B}_{\|\cdot\|_\infty}(\partial\Omega(t_0), \epsilon)$ by decomposing this in a bundle of uPA micro-processes on each of the micro-domains ϵY. In this context, during any macroscopic time range $[t_0, t_0 + \Delta t]$ that is correspondingly matched by an equal length micro-scale time span $[0, \Delta t]$ for the microdynamics, on any micro-domain ϵY, a source of uPA arises naturally at any micro-scale point $y \in \epsilon Y$ as a collective contribution not only of the uninfected cancer cells but also of the infected cancer cells and syncytia population that arrive within a given distance $\delta > 0$ with respect to y, see Figure 2. Thus, the microscale source of uPA is induced non-locally by the macro-dynamics through a *top-down link*, and this can be mathematically expressed as

$$f^{\epsilon Y}_{uPA}(y,\tau) = \frac{\int\limits_{\mathbf{B}(y,\delta)\cap\Omega(t_0} (\lambda_c c + \lambda_i i + \lambda_s s)(\sigma, t_0 + \tau)d\sigma}{\lambda(\mathbf{B}(y,\delta) \cap \Omega(t_0)} \quad (11)$$

where $\tau \in [0, \Delta t]$ and λ_c, λ_i and λ_s are the rates at which the uninfected cancer cells, the infected cancer cells and syncytia population secrete uPA, respectively. Since in the presence of this source, per unit time, the uPA molecules are assumed to exercise a random movement and are taken out of the system through binding to the inhibitor PAI-1 as well as to the receptors uPAR, the dynamics of the uPA can therefore be expressed mathematically as:

$$\frac{\partial a}{\partial \tau} = \underbrace{D_a \Delta a}_{\text{diffusion}} - \underbrace{\psi_{11} a p}_{\text{uPA/PAI-1}} + (\underbrace{\psi_{12}}_{\text{production}} - \underbrace{\psi_{13} u}_{\text{uPA/uPAR}}) f^{\epsilon Y}_{uPA}(y,\tau) \quad (12)$$

At the same time, the inhibitor PAI-1, which is produced through the activation of plasmin, is eliminated from the system dynamics after binding to uPA and, notably, through non-local binding to the surrounding ECM (more specifically, to its constituent vitronectin). This binding of PAI-1 to constituents of the surrounding tissue-scale ECM density acts therefore as an absorption term for the PAI-1 micro-dynamics, whose absorption coefficient is again mediated and induced by the macro-dynamics (enhancing this way the *top-down feedback link*) and can be formalised mathematically through the non-local expression

$$f^{\epsilon Y}_{PAI-1}(y,\tau) = \frac{\int\limits_{\mathbf{B}(y,\delta)} u(\sigma, t_0+\tau)d\sigma}{\lambda(\mathbf{B}(y,\delta))}. \quad (13)$$

where $(y,\tau) \in (\epsilon Y \cap \Omega(t_0)) \times [0, \Delta t]$. Therefore, the microdynamics of PAI-1 is governed by

$$\frac{\partial p}{\partial \tau} = \underbrace{D_p \Delta p}_{\text{diffusion}} - \underbrace{\psi_{21} a p}_{\text{uPA/PAI-1}} - \underbrace{\psi_{22} p\, f^{\epsilon Y}_{PAI-1}(y,\tau)}_{\text{PAI-1/ECM}} + \underbrace{\psi_{23} m}_{\text{production}}. \quad (14)$$

Finally, as the loss of PAI-1 due to binding to ECM has a positive feedback on plasmin, the usual source of plasmin that is mediated by the activation of uPA through binding to uPAR receptors is enhanced this way by an additional production source that corresponds to the non-local absorption term from the PAI-1 dynamics in (14). Thus, in the presence of this enhanced source, per unit time, plasmin exercises a random movement and naturally decays, and so its dynamics can be formalised mathematically as

$$\frac{\partial m}{\partial \tau} = \underbrace{D_m \Delta m}_{\text{diffusion}} + \underbrace{\psi_{31} a f^{\epsilon Y}_{uPA}(y,\tau)}_{\text{uPA/uPAR}} + \underbrace{\psi_{32} p f^{\epsilon Y}_{PAI-1}(y,\tau)}_{\text{PAI-1/ECM}} - \underbrace{\psi_{33} m}_{\text{decay}}. \quad (15)$$

Therefore, the microscopic proteolytic dynamics is given by the following 3D-reaction-diffusion-taxis system:

$$\begin{cases} \frac{\partial a}{\partial \tau} = D_a \Delta a - \psi_{11} a p + (\psi_{12} - \psi_{13} u) f^{\epsilon Y}_{uPA}(y,\tau), \\ \frac{\partial p}{\partial \tau} = D_p \Delta p - \psi_{21} a p - \psi_{22} p\, f^{\epsilon Y}_{PAI-1}(y,\tau) + \psi_{23} m, \\ \frac{\partial m}{\partial \tau} = D_m \Delta m + \psi_{31} a f^{\epsilon Y}_{uPA}(y,\tau) + \psi_{32} p f^{\epsilon Y}_{PAI-1}(y,\tau) - \psi_{33} m, \end{cases} \quad (16)$$

Finally, as we assume *"no molecular memory"* from any previous macro-micro stages, the micro-dynamics system (16) is accompanied by zero initial conditions, i.e.,

$$a(y,0) = 0, \quad p(y,0) = 0, \quad m(y,0) = 0, \quad \forall y \in \epsilon Y.$$

Furthermore, as we there is no molecular transport across the interface of the micro-domains ϵY, we assume also zero Neumann boundary conditions, i.e.,

$$\left.\frac{\partial a}{\partial n}\right|_{\epsilon Y} = 0; \quad \left.\frac{\partial p}{\partial n}\right|_{\epsilon Y} = 0; \quad \left.\frac{\partial m}{\partial n}\right|_{\epsilon Y} = 0.$$

As discussed in detail [21, 22], the cross-interface transport exercised by the uPA system within each micro-domain ϵY (captured in (16)) leads to a pattern of degradation of the peritumoural ECM within $\epsilon Y \setminus \Omega(t_0)$ resulting into an important *bottom-up* feedback to the tissue-scale that ultimately dictates the way the macro-scale tumour boundary is relocated, as illustrated in Figure 2. Thus, to capture this feedback link, we follow the multiscale approach introduced in [21] and further discussed in [22],

which enables us to explore the regions of significant ECM degradation within $\epsilon Y \setminus \Omega_{t_0}$ and ultimately to determine a unique direction of movement $\eta_{\epsilon Y}$ and a displacement magnitude $\xi_{\epsilon Y}$ that indicates the way the boundary captured by ϵY, namely $\epsilon Y \cap \partial\Omega(t_0)$ is progressed further in the domain (please see [21, 22] for full details). This enables us to capture the choreographic movement of the portion of the boundary $\epsilon Y \cap \partial\Omega(t_0)$ and to represented this at macro-scale through the movement of the *central boundary point of* $\epsilon Y \cap \partial\Omega(t_0)$ to a new position in the direction $\epsilon Y \cap \partial\Omega(t_0)$ by a displacement magnitude $\xi_{\epsilon Y}$. Finally, under the incidence of this bottom-up feedback induced by the tumour invasive edge micro-dynamics over each time interval $[t_0, t_0 + \Delta t]$, the boundary of the tumour $\Omega(t_0)$ is eventually progressed into a newly relocated and eventually expanded shape $\Omega(t_0 + \Delta t)$ where the full multiscale dynamics is continued on the subsequent macro-micro stage $[t_0 + \Delta t, t_0 + 2\Delta t]$, as schematically illustrated in Figure 2.

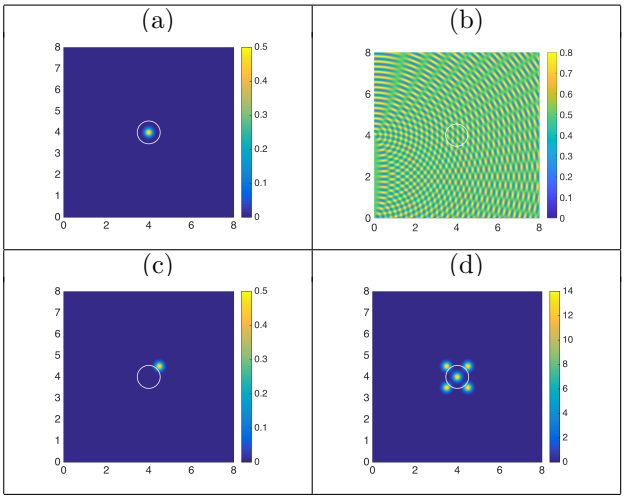

Figure 3: *Initial Conditions: (a) uninfected cancer cells density; (b) ECM density; (c) OV density (one initial dose) and (d) OV density (five initial doses). The white line indicates the boundary of the total tumour cells (uninfected & infected densities).*

3. Multiscale Numerical Simulations for Macro-Dynamics Cases (8)-(10)

Starting from the two-scale computational framework that was previously developed in [20] for the case that was not considering syncytia structures formation (which was based on the initial two-scale framework proposed in [21]), we developed that framework further to cope with the new context of multiscale dynamics of cancer-virus interactions in the presence of syncytia structures formation. Similar to the initial framework (introduced in [21]), the extended multiscale numerical scheme that we developed and use here combines predictor-corrector finite differences for the macro-dynamics with quadrilateral finite element approach for micro-dynamics. Further, as detailed in [21], the internal macro-mesh is extended with additional mesh points when the boundary is relocated (which are activated from a silent background mesh on the maximal tissue cube Y) Finally, since the development of this extended numerical scheme required a discretisation strategy similar to that used in the non-syncytia case (considered in [20]), we did not include that here and instead, for details of the main implementation steps, we refer the reader to [20, 21].

3.1. Initial Conditions for the Macro-Micro Model

The initial distribution of the uninfected cancer cells (which form a tumour localised in the middle a computational domain $Y = [0, 8] \times [0, 8]$) is given by:

$$c(x,0) = \frac{\left(exp(-\frac{\|x-(4,4)\|_2^2}{\sqrt{\Delta x \Delta y}}) - exp(-28.125)\right)\theta_1(x)}{2},$$

where $\theta_1(x) := \chi_{\mathbf{B}((4,4),0.5-\gamma)} * \psi_\gamma$, with ψ_γ a Gaussian mollifier that enables a smooth transition to zero outside a radius of 0.5 of the ball $\mathbf{B}((4,4),0.5)$, as shown Figure 3-(a).

Since the oncolytic virus is introduced into the system at the start of the simulations, it makes sense to assume that at this time (i.e., $t = 0$) there are no virus-infected and syncytia cancer cells:

$$i(x,0) = 0, \quad \text{and} \quad s(x,0) = 0.$$

Regarding the virus, we assume that this is injected at tumour site (at the start of the simulations), via a single or multiple insertion points [38, 39, 40]. For the baseline simulations, we choose a single insertion point, as described in Figure (3)(c) and given by the expression

$$v(x,0) = \frac{\left(exp(-\frac{\|x-(4.5,4.5)\|_2^2}{\sqrt{\Delta x \Delta y}}) - exp(-28.125)\right)\theta_2(x)}{2},$$

where $\theta_2(x) := \chi_{B((4.5,4.5),0.5-\gamma)} * \psi_\gamma$. However, for an improved viral therapy outcome scenario (given that the initial tumour lesion is quite spread over space – see Figure (3)(a)), we inject five virus doses at different positions inside the tumour, as shown in Figure (3)(d):

$$\begin{aligned} v(x,0) = & \\ & \sum_{i,j\in\{-1,1\}} 0.5\Big(exp(-\tfrac{\|x-(4+0.5i,4+0.5j)\|_2^2}{\sqrt{\Delta x \Delta y}}) - exp(-28.125)\Big)\theta_{i,j}(x) \\ & + 0.5\Big(exp(-\tfrac{\|x-(4,4)\|_2^2}{\sqrt{\Delta x \Delta y}}) - exp(-28.125)\Big)\,\theta_1(x), \end{aligned}$$

where $\theta_{i,j}(x) := \chi_{B((4+0.5i,4+0.5j),0.5-\gamma)} * \psi_\gamma$, $\forall i, j \in \{-1, 1\}$.

Finally, since the ECM is naturally heterogeneous, we considered here the following ECM initial condition :

$$u(x,0) = \frac{1 + 0.3sin(4\pi \|x\|_2) + sin(4\pi \|(4,0) - x\|_2)}{2}.$$

Further insights upon the impact that the choice of the ECM initial conditions has on the overall tumour evolution are discussed in Appendix A, where we explore the

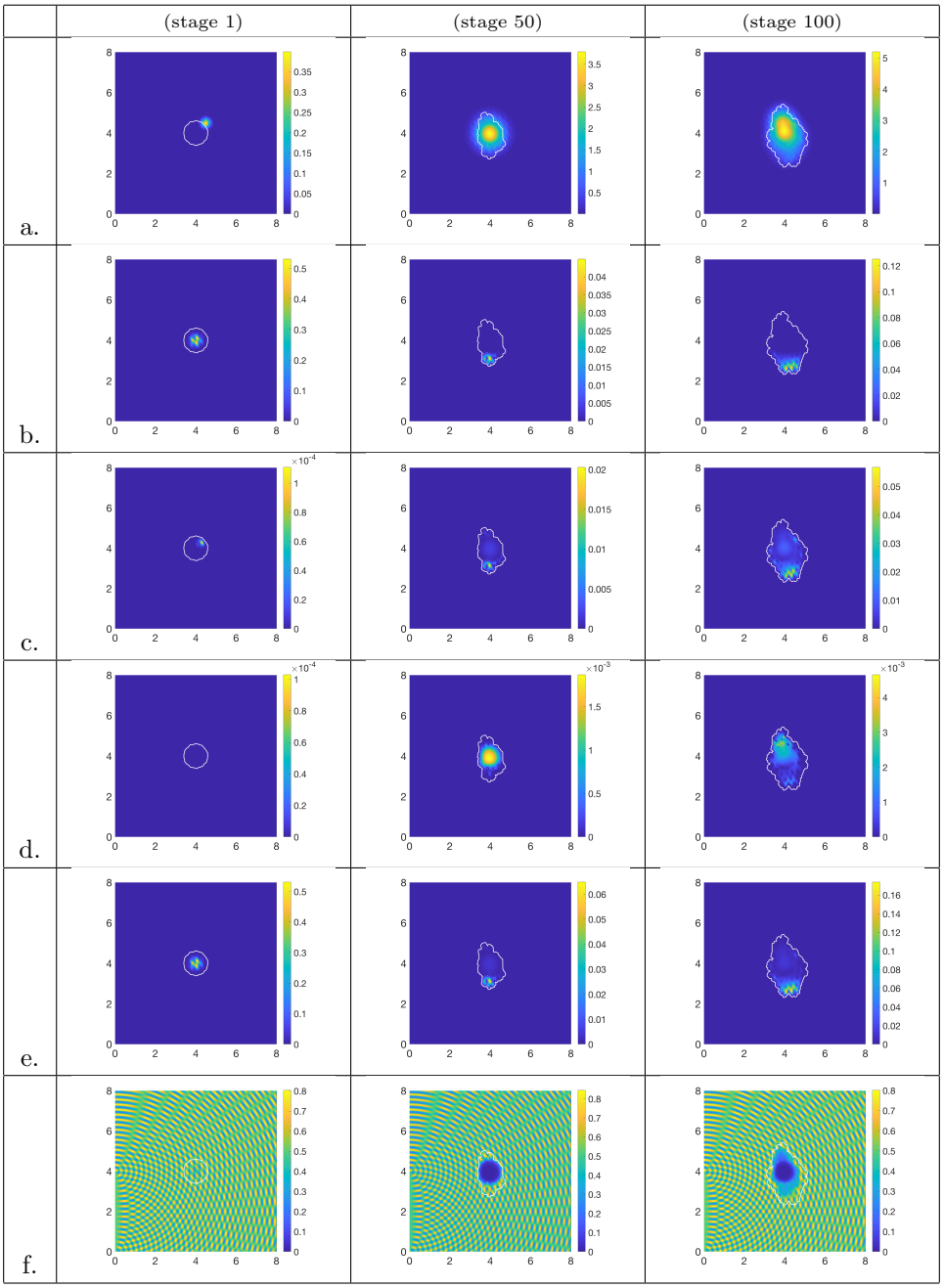

Figure 4: *Multi-scale simulation results for macro-dynamics syncytia system* (8) *at three macro-micro stages (1,50 and 100) for the baseline parameter values from Table 1, showing: a. virus density; b. uninfected cancer cells density; c. infected cancer cells density; d. syncytia cancer cells density; e. total cancer cells density and f. ECM density.*

sensitivity of the viral treatment of the tumour with respect to the level of heterogeneities within the ECM.

Regarding the initial conditions at the microscale: we assume that the enzymes are produced only by the cancer cells at macroscale level (and passed nonlocally to the microscale), and there are no other pre-existing enzymes in the peritumoural interface. Thus, we always consider zero initial conditions for enzymes at the microscale.

3.2. Parameters

To simplify the presentation of the numerical results, in the following two tables we summarise the baseline parameter values used in the simulations.

3.3. Results

To investigate the different scenarios discussed in the previous section (regarding the tumour-OV interactions in the presence of cells syncytium) we start our numerical

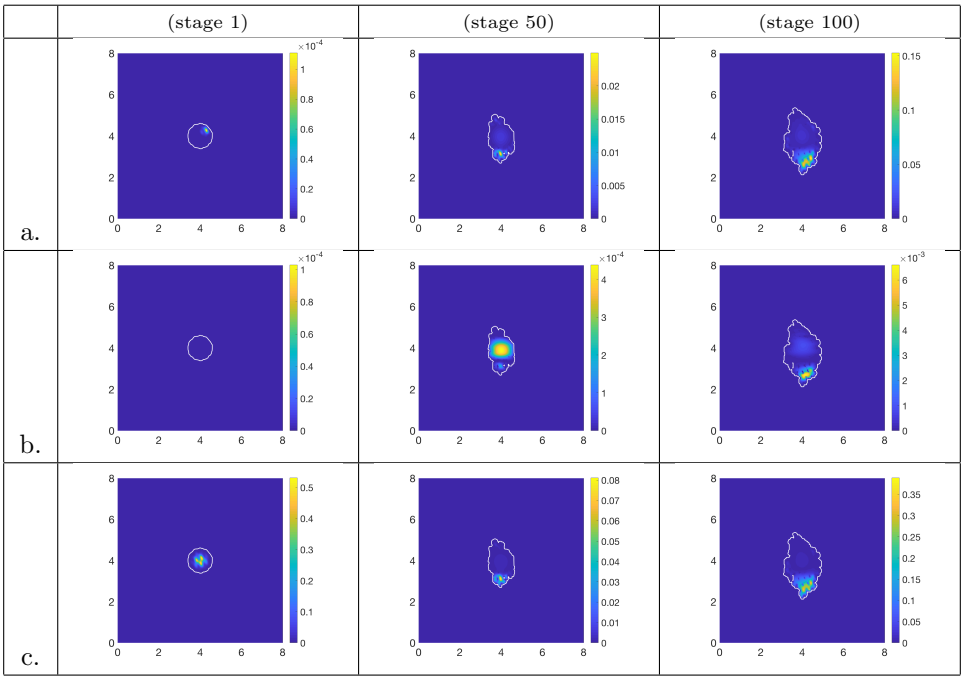

Figure 5: *Multi-scale simulation results for macro-dynamics syncytia system* (9) *in the case of* $D_s = D_i$ *at three macro-micro stages (1,50 and 100) for the baseline parameter values from Table 1, showing: a. infected cancer cells density; b. syncytia cancer cells density and c. total cancer cells density.*

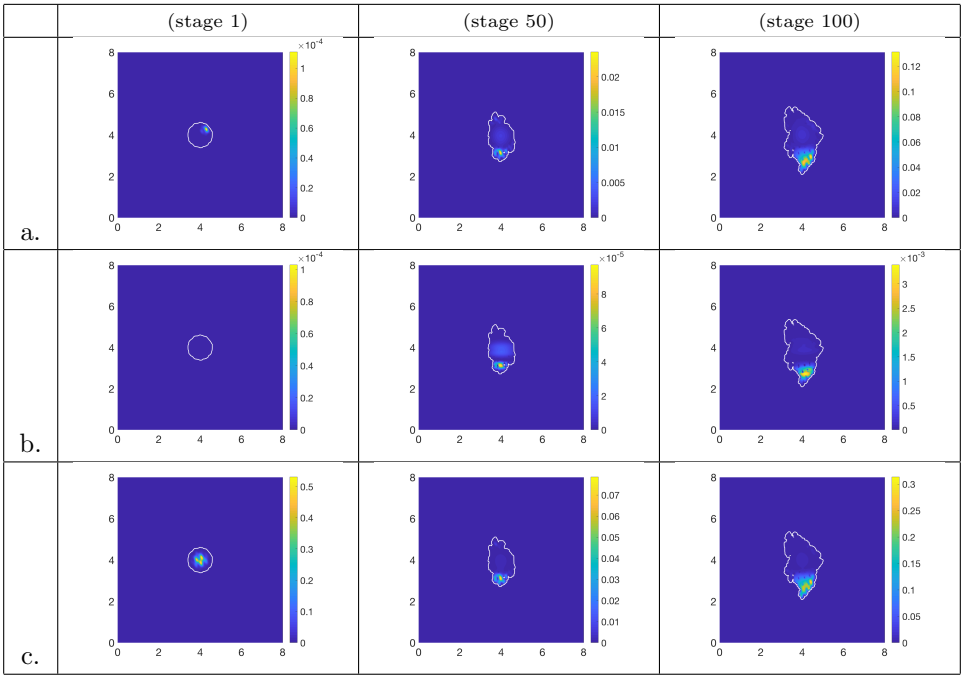

Figure 6: *Multi-scale simulation results for macro-dynamics syncytia system* (9) *in the case of* $D_s = D_i/4$ *at three macro-micro stages (1,50 and 100) for the baseline parameter values from Table 1, showing: a. infected cancer cells density; b. syncytia cancer cells density and c. total cancer cells density.*

simulations with the baseline parameters summarised in Tables 1, 2.

We start our numerical investigation of the multiscale moving-boundary model proposed in this study by focusing on the three cases of syncytia movement/lack-of-movement. For the first case, described mathematically by the macro-dynamics (8), we assume that syncytia structures do not have any movement ability (i.e., neither diffusive nor haptotactic movement), but they can still play a role in the remodelling and degradation of ECM compo-

Parameter	Value	References
D_c	0.00675	[41]
D_i	0.0054	[41]
D_s	0.0027	$\frac{D_i}{2}$
D_v	0.0036	[41]
η_c	2.85×10^{-2}	[22]
η_i	2.85×10^{-2}	[22]
η_s	2.85×10^{-3}	Estimated
η_v	2.85×10^{-3}	[20]
μ_1	0.25	[22]
ρ	79×10^{-3}	[41]
κ	158×10^{-3}	$\kappa > \rho$, [13], [42]
δ_i	0.05	[41]
δ_s	0.05	$(\delta_s = \delta_i)$ Estimated
δ_v	0.025	[41]
α_c	0.15	[22]
α_i	0.075	[20]
α_s	0.0375	$(\frac{\alpha_c}{4})$ Estimated
μ_2	0.015	[20]
b_i	2	[20]
b_s	2	$(b_s = b_i)$ Estimated
p_0	0.5	50% Probability
λ_c	0.8	[20]
λ_i	0.4	[20]
λ_s	0.4	$(\lambda_s = \lambda_i)$ Estimated

Table 1: *Baseline parameters values for the macroscopic models.*

Parameter	Value
D_a	2.5×10^{-3}
D_p	3.5×10^{-3}
D_m	4.91×10^{-3}
ψ_{11}	0.75
ψ_{12}	0.215
ψ_{13}	0.3
ψ_{21}	0.75
ψ_{22}	0.55
ψ_{23}	0.5
ψ_{31}	0.11
ψ_{32}	0.75
ψ_{33}	0.5

Table 2: *Summary of parameter values for the microscopic model component. All parameters for this system are taken from the reference [22].*

nents on the tumour region $\Omega(t)$. The dynamics of the various macroscale model components is presented in Figure 4, where we show (for three different micro-macro stages, 1, 50 and 100): the virus density (row a.), the density of uninfected cancer cells (row b.), the density of infected cancer cells (row c.), the density of syncytia cancer cells (row d.), total cancer cells density (row e.), and ECM density (row f.). We note that in this case, the syncytia structures form mainly in those tumour regions characterised by lower tumour cell densities, while the single infected cells are mainly in those regions characterised by higher tumour cell densities.

For the second case, described mathematically by the macro-dynamics (9), we assume that syncytia cells can move randomly inside the macroscopic domain, but they do not show haptotactic migration towards regions of higher ECM levels. To investigate the effect of this random motility of syncytia structures, we perform simulations with different syncytia diffusion coefficients D_s (with respect to D_i - the diffusion coefficient of single infected cells). Thus, in Figure 5 we investigate the situation $D_s = D_i$; in Figure 6 we investigate the situation $D_s = D_i/4$; and in Figure 7 we investigate the situation $D_s = 4D_i$. We observe here that lower D_s compared to D_i (i.e., $D_s = D_i/4$) leads to syncytia structures localised also in the non-infected part of the tumour, which causes an overall reduction in tumour size and tumour spread (as the invasion boundary is shrinking). In contrast, increasing D_s compared to D_i (i.e., $D_s = 4D_i$) leads to an increase in tumour size and tumour spread. It is possible that lower syncytia motility leads to more localised tumour killing and localised release of virus particles, while larger syncytia motility leads to a wider spread of the virus particles, which also increases their probability of elimination. In Figure 8 we summarise all these results by showing the effect of syncytia random motility on: (a) total tumour mass (i.e., uninfected+infected+syncytia); (b) tumour invasion area; and the evolution of the ration between the total tumour mass and the tumour invasion area

Next, we return to the case $b_s = b_i$ and $\delta_s = \delta_i$, and show an example of significant tumour reduction when we decrease the parameters associated with the proteolytic enzymes (see Table 3), which are expected to lead to smaller enzymatic transport across the tumour interface, ultimately resulting in peritumoural ECM degradation. This results in slower tumour invasion, which enables the syncytia and infected cells to be more effective at cancer cell elimination on tumour domain $\Omega(t)$. This behaviour is depicted in Figure 15. In Figure 16 we compare – in terms of total tumour mass and tumour invasion area – this improved therapy scenario versus the baseline scenario described by the parameter values listed in Table 1.

Finally, we investigate the third case, described mathematically by the macro-dynamics (10), where we assume that syncytia cancer cells not only diffuse randomly but also move haptotactically towards higher ECM gradients. As before, we investigate numerically the effects of various syncytia haptotactic velocities η_s (as compared with the haptotactic velocities of single infected cancer cells η_i, and the velocities of virus particles η_v). Figure 9 summarises these effects on: (a) total tumour size; (b) tumour invasion area for the following two sub-cases: (i) $\eta_s = \eta_i = 2.85 \times 10^{-2}$ and (ii) $\eta_s = \eta_v = 2.85 \times 10^{-3}$; and the evolution of the ration between the total tumour mass and the tumour invasion area. Note that case (ii), where

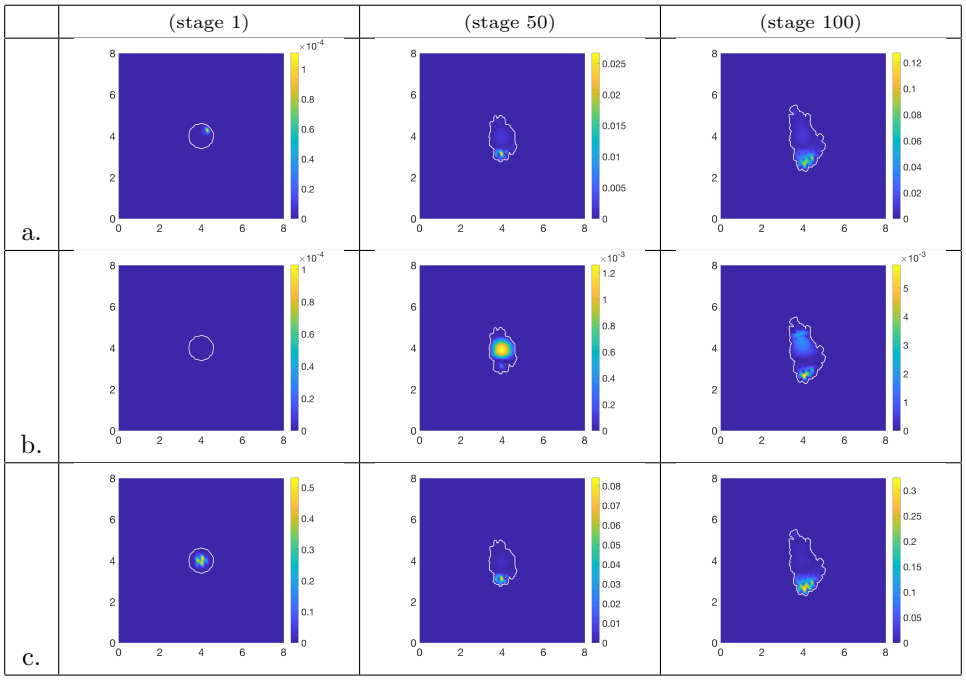

Figure 7: *Multi-scale simulation results for macro-dynamics syncytia system* (9) *in the case of* $D_s = 4D_i$ *at three macro-micro stages (1,50 and 100) for the baseline parameter values from Table 1, showing: a. infected cancer cells density; b. syncytia cancer cells density and c. total cancer cells density.*

Parameter	Value	References
D_c	0.00675	[41]
D_i	0.0054	[41]
D_s	0.000675	Estimated
D_v	0.0036	[41]
η_c	2.85×10^{-2}	[22]
η_i	2.85×10^{-2}	[22]
η_s	2.85×10^{-3}	Estimated
η_v	2.85×10^{-3}	[20]
μ_1	0.25	[22]
ρ	395×10^{-3}	[20]
κ	2ρ	$\kappa > \rho$, [13], [42]
δ_i	0.0125	[20]
δ_s	0.0125	$(\delta_s = \delta_i)$ Estimated
α_c	0.3	[20]
α_i	0.15	[20]
α_s	0.075	$(\frac{\alpha_c}{4})$ Estimated
μ_2	0.015	[20]
b_i	3	[20]
b_s	3	$(b_s = b_i)$ Estimated
p_0	0.75	Estimated
δ_v	0.025	[41]
λ_c	0.8	[20]
λ_i	0.4	[20]
λ_s	0.4	$(\lambda_s = \lambda_i)$ Estimated

Table 3: *Parameter values list for the improved tumour suppression results, as summarised in Figure (16).*

$\eta_s = \eta_v < \eta_i$, leads to a slightly better tumour outcome in terms of both tumour mass and invasion area.

Having investigated the role of syncytia's diffusive/haptoctatic speeds on tumour growth and spread, we next focus on the impact of the fusion failure probability p_0 on the overall oncolytic therapy. (Note that higher p_0 means higher numbers of individual OV-infected cancer cells i, and lower numbers of syncytia structures s). In Figures 10, 11 and 12 we investigate the effect of three failure levels of syncytia fusion probability: $p_0 = 50\%$, $p_0 = 25\%$ and $p_0 = 75\%$, respectively. By comparing the results in these three figures we can conclude that higher p_0 values are associated with lower syncytia densities and lower tumour sizes. The anti-tumour effect of higher p_0 probabilities can be seen more clearly in Figure 13, where we show the evolution of total tumour mass and tumour invasion area as well as the evolution of the ratio of total tumour masses to tumour invasion area over macro-micro stages 1 – 100.

This unexpected outcome might be caused by the assumption that $b_s = b_i$ (i.e., both individually-infected tumour cells and syncytia structure burst at the same rates to release new virus particles), and $\delta_s = \delta_i$ (i.e., both individually-infected tumour cells and syncytia structures die at the same rates). However, it makes sense to assume that syncytia live longer than the individually-infected cells [43], and that each syncytium has a higher viral yield compared to the yield of a single infected cell. Thus, in Figure 14 we investigate the anti-tumour/pro-tumour effects of higher syncytia burst rates ($b_s = 1.5b_i$) and lower

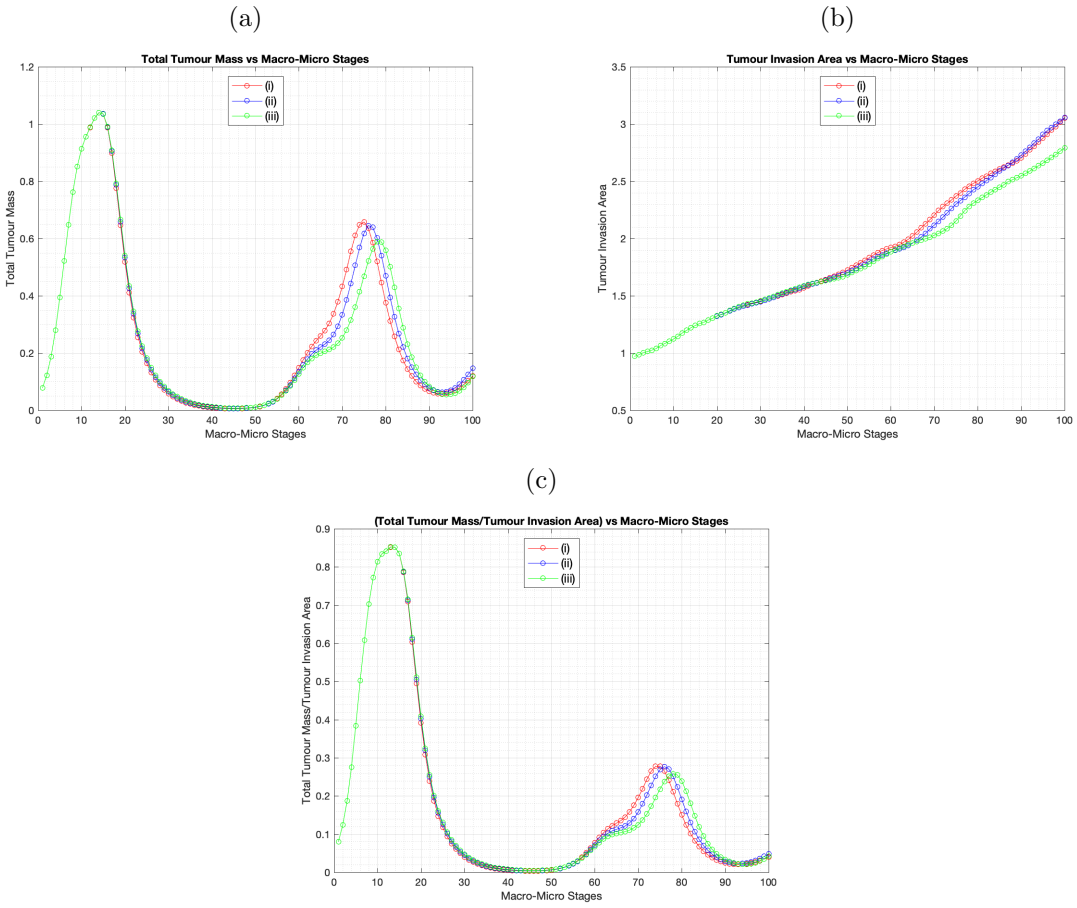

Figure 8: *Comparison of: (a) total tumour masses evolution versus macro-micro stages 1 – 100 for the macro-dynamics case* (9) *for various random diffusion scenarios of syncytia cancer cells; (b) tumour invasion area versus macro-micro stages 1 – 100 for the macro-dynamics case* (9) *for various random diffusion scenarios of syncytia cancer cells; and (c) the evolution of the ratio of total tumour masses to tumour invasion area over macro-micro stages 1 – 100 for the macro-dynamics case* (9) *for various random diffusion scenarios of syncytia cancer cells. (i)* $D_s = 4D_i$*; (ii)* $D_s = D_i$*; (iii)* $D_s = D_i/4$*.*

syncytia death rates ($\delta_s = \frac{\delta_i}{5}$), and compare the results with the ones for the above case (i.e., $b_s = b_i$, $\delta_s = \delta_i$). It is clear that higher probabilities of syncytium formation (i.e., lower p_0) lead to faster tumour death when $b_s > b_i$ and $\delta_s < \delta_i$.

4. Extension of Macro-Dynamics Case (10) to Include Density-Dependent Syncytia Diffusion

The previously-discussed cases assumed that syncytia diffusion is constant. However, given the size of this giant multi-nucleated structure, it is likely that its motility is influenced by the density of ECM, as well as the density of fusogenic oncolytic viruses (as more viruses could lead to larger syncytia, which extend larger pseudopods to move [9]). In the following we generalise the macro-dynamics described in model (10) by assuming that syncytia diffusion coefficient is density dependent:

$$\begin{cases} \frac{\partial c}{\partial t} = D_c \Delta c - \eta_c \nabla \cdot (c \nabla u) + \mu_1 c(1-c) - \rho c v - \kappa c i, \\ \frac{\partial i}{\partial t} = D_i \Delta i - \eta_i \nabla \cdot (i \nabla u) + \rho c v + p_0 \kappa c i - \delta_i i, \\ \frac{\partial s}{\partial t} = \left(D_s \frac{v}{f_s(u,v)} \right) \Delta s - \eta_s \nabla \cdot (s \nabla u) + (1-p_0) \kappa c i - \delta_s s, \\ \frac{\partial u}{\partial t} = -u(\alpha_c c + \alpha_i i + \alpha_s s) + \mu_2 u(1-u-c-i-s), \\ \frac{\partial v}{\partial t} = D_v \Delta v - \eta_v \nabla \cdot (v \nabla u) + b_i i + b_s s - \rho c v - \delta_v v. \end{cases} \tag{17}$$

Note that this model reduces to case (10) if we choose $f_s(u,v) = v$. In the following we consider two examples for f_s (both leading to a saturated diffusion coefficient for the syncytia structures):

i. $f_s(u,v)$ depends only on OV, and the dependence is linear:

$$f_s(u,v) = v + 1; \tag{18}$$

ii. $f_s(u,v)$ depends on both OV and ECM, and the de-

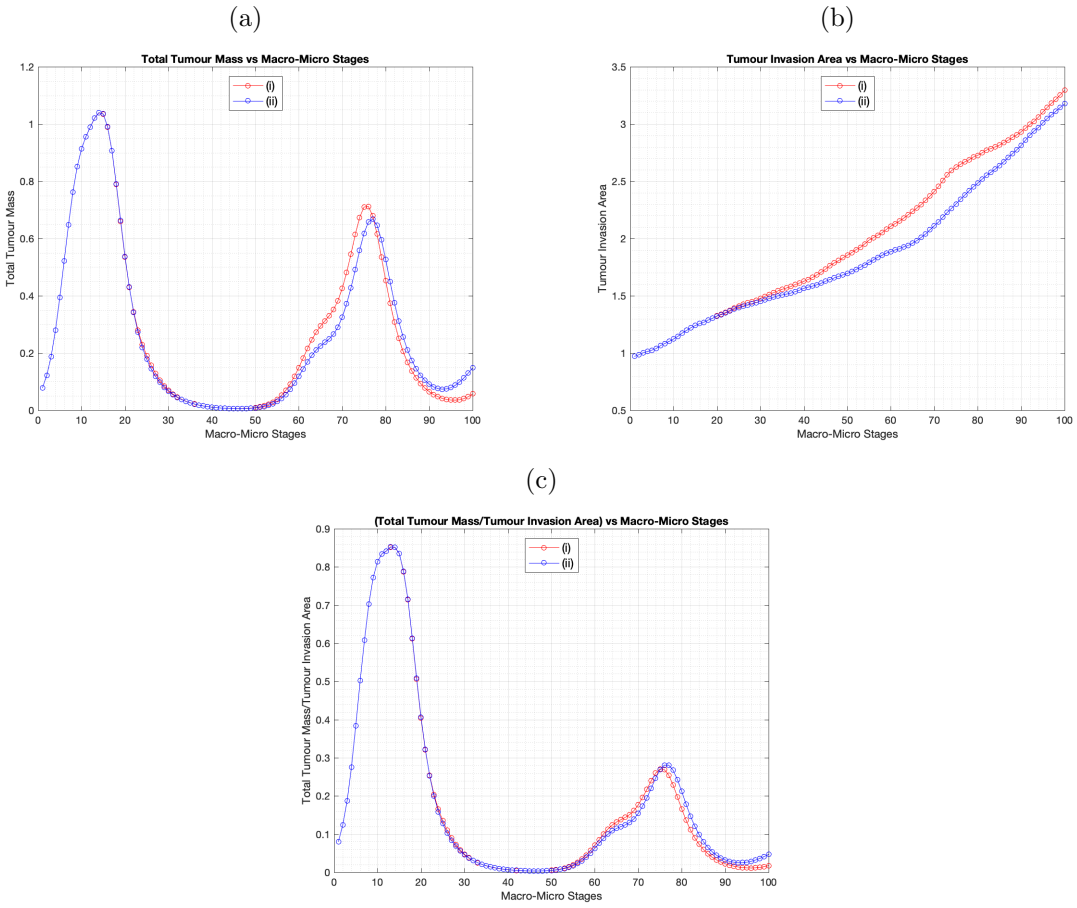

Figure 9: *(a) Comparison of total tumour masses evolution over macro-micro stages 1 – 100 for the macro-dynamics case* (10) *for various haptotactic rates of syncytia cancer cells ECM gradients. (b) Comparison of tumour invasion area over macro-micro stages 1 – 100 for the macro-dynamics case* (10) *for various haptotactic rates of syncytia cancer cells towards ECM gradients. (c) Comparison of the evolution of the ratio of total tumour masses to tumour invasion area over macro-micro stages 1 – 100 for the macro-dynamics case* (10) *for various haptotactic rates of syncytia cancer cells ECM gradients. (i)* $\eta_s = \eta_i$*; (ii)* $\eta_s = \eta_v$*.*

pendence is linear:

$$f_s(u, v) = u + v + 1. \tag{19}$$

In Figure 18 we show the evolution of the total tumour mass (for the baseline parameters listed in Table (1)) over 100 micro-macro stages. We compare the baseline dynamics generated by model (10) (case (a) described by the red curve) with the dynamics generated by model (17)+(18) (case (b) described by the blue curve), and by model (17)+(19) (case (c) described by the green curve). Overall, the model with the density-dependent syncytia diffusion shows less tumour growth and smaller tumour invasion area during the later stages of tumour dynamics compared with the baseline model (with constant diffusion). This tumour reduction can be explained by the fact that syncytia diffusion (which depends on OV and ECM spatial distribution) leads to the accumulation of syncytia structures in areas with uninfected and infected tumour cells (the infected tumour cells releasing more OV), which ultimately causes more tumour destruction. We also note that there is no significant difference between the model dynamics with f_s described by either equations (18) or (19). For a visual description of the effect of density-dependent syncytia diffusion on the spatial distribution of total tumour (uninfected+infected+syncytia cells) at different micro-macro simulation stages please see Figure 17.

5. Summary and Discussions

In this study, we extended a multi-scale moving boundary model for oncolytic cancer virotherapy introduced in [20], by considering a fusogenic virus that can form syncytia structures (which have been shown experimentally to improve tumour reduction and control [7, 8]). The presence of syncytia not only changes the macro-dynamics with respect to the cases studied in [20], but given the link across the scales (from macro to micro) detailed in Section 2.2 that involves this time also the syncytia cells, this also influences the micro-dynamics of the proteolytic activity that takes place along the tumour invasive edge. In turn, this altered proteolitic micro-dynamics has direct impact

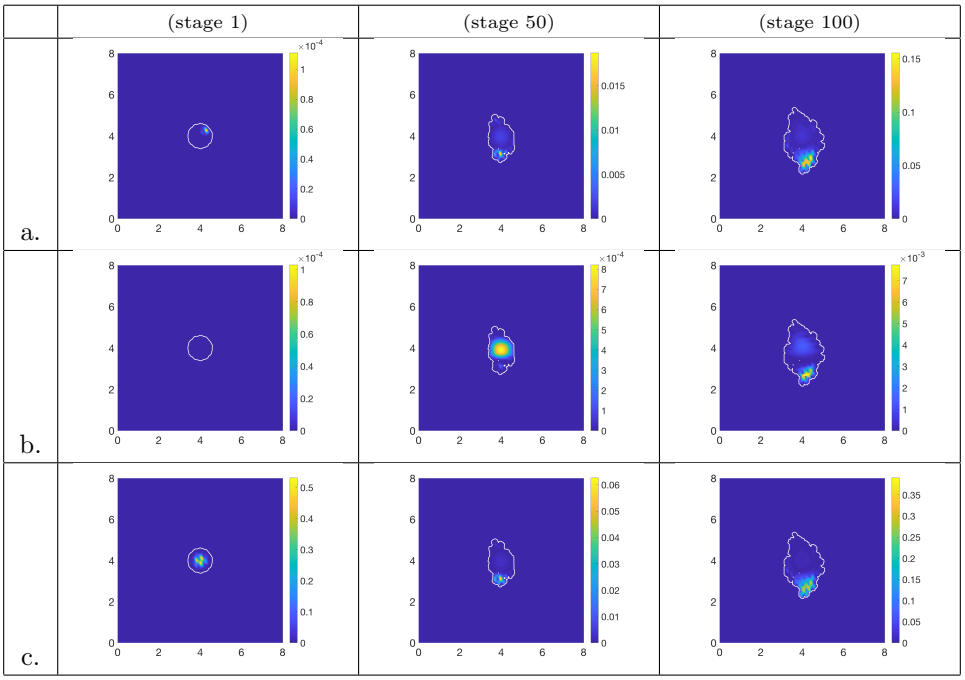

Figure 10: *Multi-scale simulation results for macro-dynamics syncytia system* (10) *in the case of 50% fusion failure probability* ($p_0 = 0.5$) *at three macro-micro stages (1,50 and 100) for the baseline parameter values from Table 1, showing: a. infected cancer cells density; b. syncytia cancer cells density and c. total cancer cells density.*

upon the progression of the tumour as well as upon the changes of its morphology, leading to a different tumour behaviour than the one observed in [20]. Further, we used this new multiscale model to investigate various hypotheses regarding the movement of these syncytia and their interactions with the tumour microenvironment across different scales. The macroscale interactions focused on the dynamics of (infected and uninfected) cancer cells, syncytia structures, virus particles and the surrounding extracellular matrix (ECM), while the microscale interactions focused on the degradation of ECM by enzymes produced by the tumour cells (see Figure 2).

Using a computational approach, we investigated different assumptions regarding the macroscale dynamics of syncytia structures: from the anti-tumour/pro-tumour effects of various diffusive and advective abilities of syncytia (see Figures 4-9), to the anti-tumour/pro-tumour effects of different probabilities of syncytia forming (see Figures 10-13). The results suggested that lower syncytia motility compared to single infected cells (i.e., $D_s < D_i$, and $\eta_s < \eta_i$) could lead to better anti-tumour outcomes. Moreover, higher probabilities (p_0) of fusogenic viruses failing to form syncytia seemed to lead to better anti-tumour outcomes. These results were likely caused by the specific baseline parameter values listed in Table 1, which were chosen to match the parameter values from [20].

To explain these unexpected results, we also investigated the combined effect of syncytia-forming probability and different death rates for the infected cells and syncytia (δ_i, δ_s), as well as different virus burst rates for the infected cells and syncytia (b_i, b_s); see Figure 14. The results suggested that more realistic parameter values (i.e., $b_s > b_i$, $\delta_s < \delta_i$, and $p_0 = 0.25 \Rightarrow (1 - p_0) = 0.75$) lead to better anti-tumour outcomes compared to the baseline case. We also investigated the effect of decreasing the values of some parameters associated with the proteolytic enzymes (i.e., lower enzymatic transport across tumour interface), and observed that this lead to a slower tumour invasion and faster tumour elimination by the infected cells and syncytia; see Figures 15 - 16. We can conclude from here that the outcome of the oncolytic therapy does not depend only on various macroscopic cell and virus particle dynamics, but also on the microscopic dynamics of enzymes involved in ECM degradation.

Panels (a) of Figures 8, 9, 13, 14 and 16 suggest that between the macro-micro stages 40 and 50 the tumour mass becomes very small. This would suggest that there is the possibility of tumour extinction by oscillations (see, although in another context, [44, 45]). However, our model is deterministic, and as such it cannot capture: i) stochastic behaviours when the tumor mass is very small; ii) extrinsic stochastic fluctuations, which is a delicate matter in tumour modelling, see [46, 47].

Finally, given that the syncytia structures are very large, their movement might be impacted by the density of ECM and/or the density of fusogenic virus particles. Thus, we investigated numerically the possibility that the random motility of these syncytia is not constant but depends on these densities (see equations (17)-(19)). The results in Figures 17 - 18 suggested that the assumption of density-

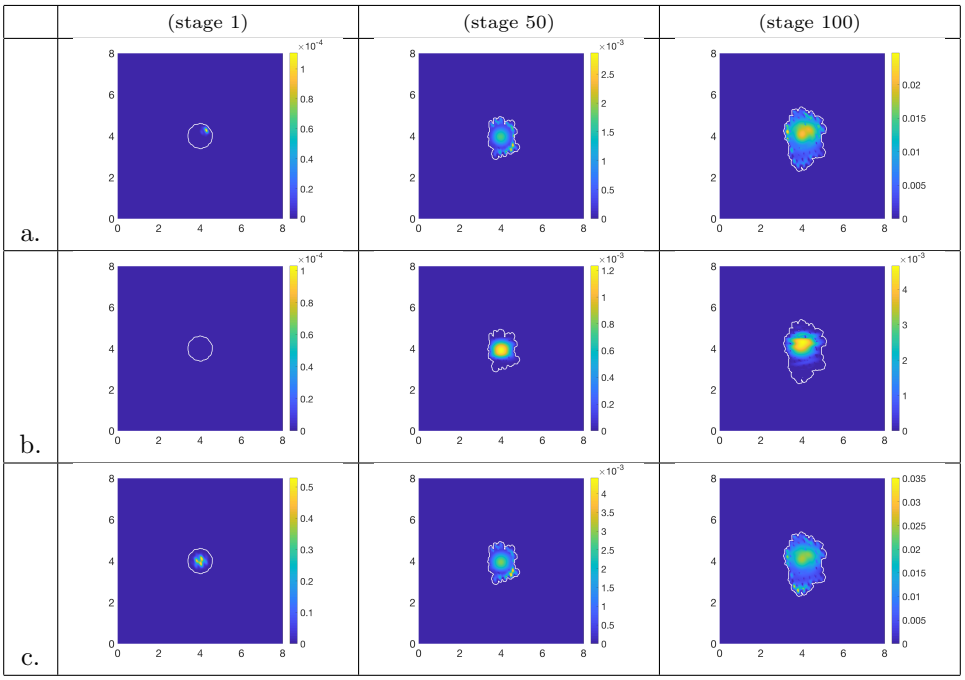

Figure 11: *Multi-scale simulation results for macro-dynamics syncytia system* (10) *in the case of 25% fusion failure probability* ($p_0 = 0.25$) *at three macro-micro stages (1,50 and 100) for the baseline parameter values from Table 1, showing: a. infected cancer cells density; b. syncytia cancer cells density and c. total cancer cells density.*

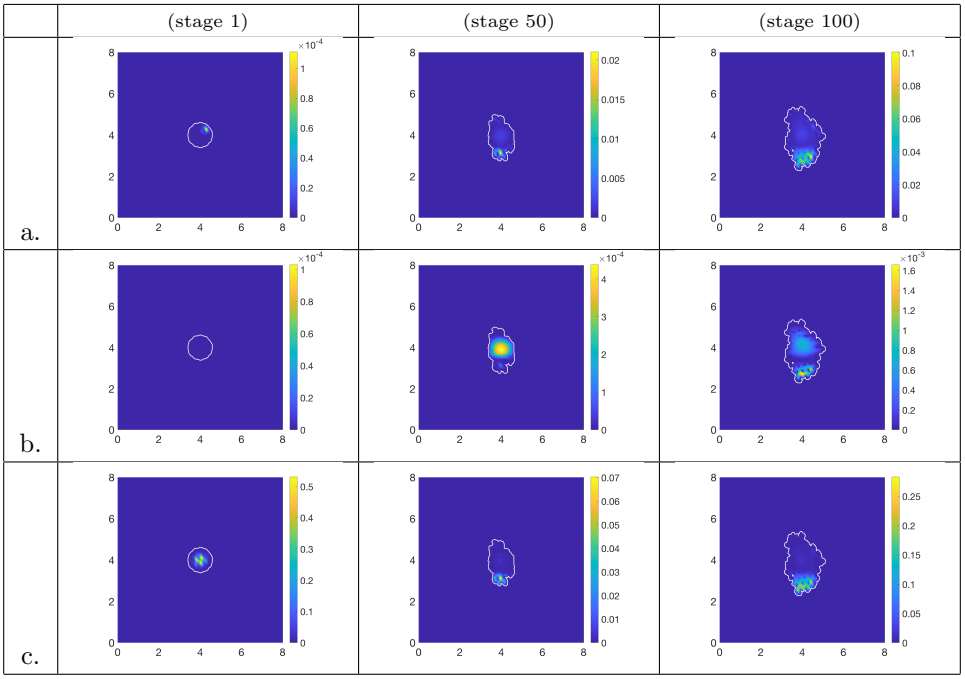

Figure 12: *Multi-scale simulation results for macro-dynamics syncytia system* (10) *in the case of 75% fusion failure probability* ($p_0 = 0.75$) *at three macro-micro stages (1,50 and 100) for the baseline parameter values from Table 1, showing: a. infected cancer cells density; b. syncytia cancer cells density and c. total cancer cells density.*

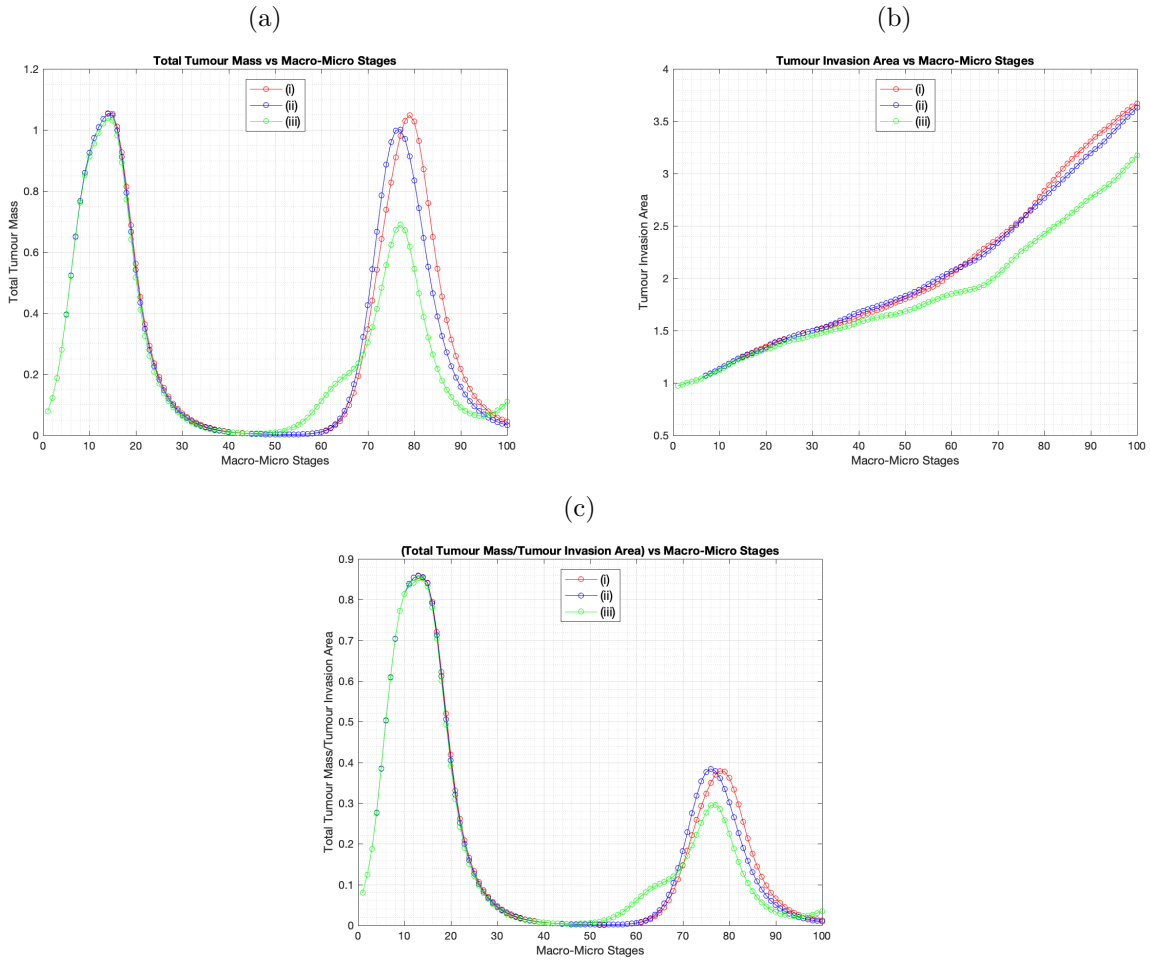

Figure 13: *(a) Comparison of total tumour masses evolution over macro-micro stages 1 – 100 for the macro-dynamics case* (10) *for various fusion failure probabilities* p_0*. (b) Comparison of tumour invasion area over macro-micro stages 1 – 100 for the macro-dynamics case* (10) *for various fusion failure probabilities* p_0*. (c) Comparison of the evolution of the ratio of total tumour masses to tumour invasion area over macro-micro stages 1 – 100 for the macro-dynamics case* (10) *for various fusion failure probabilities* p_0*. (i)* $p_0 = 0.25$*; (ii)* $p_0 = 0.50$*; (iii)* $p_0 = 0.75$*.*

dependent syncytia diffusion (versus constant diffusion) can impact the outcome of the oncolytic therapy. For the baseline parameter values shown in Table 1 the density-dependent diffusion lead to lower long-term tumour sizes and smaller tumour invasion areas, since the ECM density stopped the fast spread of syncytia, thus allowing the viruses to be more successful at killing the tumour cells.

A global multiscale analysis for this multiscale moving-boundary framework in its entirety remains an open problem. However, questions regarding the local existence and uniqueness of the macro- and micro-dynamics, while exploring the top-down link in between, are currently in preparation and form the subject of a separate work. Finally, on the numerical side, while discussions and early tests concerning of the robustness have been successfully carried out in [21] where this multiscale moving boundary framework has been initially introduced, further investigations are still needed to establish an overall multiscale numerical consistency concept for this multiscale computational platform in its entirety.

We conclude this discussion by emphasising that while cell-fusion events are very important in cell biology (in both health and disease), their roles on the spread of viral infections are not always fully understood [12]. In this study we formulated and tested computationally some hypotheses regarding the importance of various syncytium-related parameters on the spread of oncolytic viral infection and tumour reduction/elimination. One major limitation is the lack of experimental data to validate the modelling. It is however our hope that the hypotheses formulated in this paper will stimulate suitable biological experimental work that would challenge and sick to validate our computational findings. Thus, the next step would be to combine this multiscale moving-boundary mathematical framework with *in vitro* or *in vivo* experiments for oncolytic viral therapies for cancer (see, for example, the spatial data from [48] on oncolytic virus spread), to try to approximate some parameter ranges and thus to make

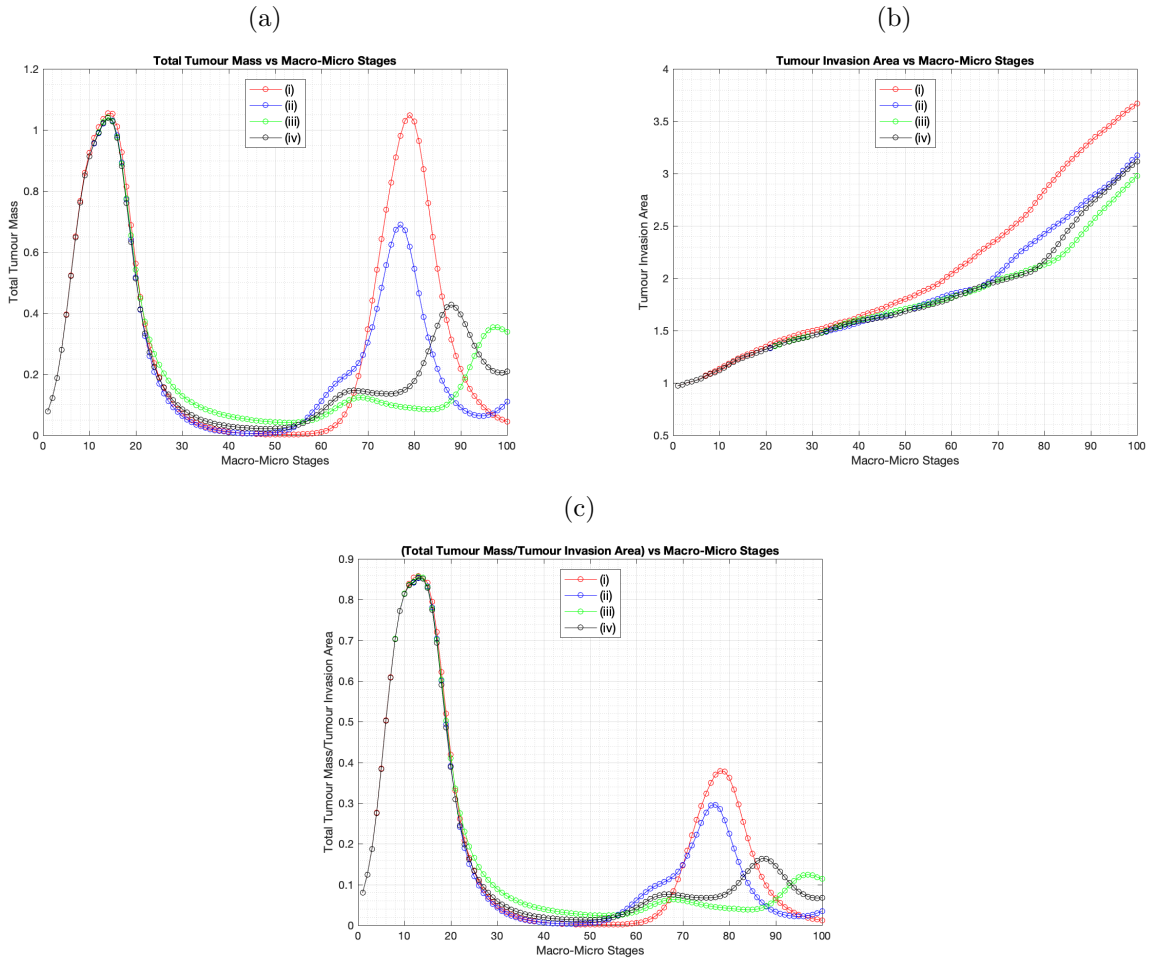

Figure 14: *(a) Comparison of total tumour masses evolution over macro-micro stages 1 – 100 for the macro-dynamics case* (10) *for various fusion probabilities* p_0*. (b) Comparison of tumour invasion area over macro-micro stages 1 – 100 for the macro-dynamics case* (10) *for various fusion failure probabilities* p_0 *with respect to different values of* b_s *and* δ_s*. (c) Comparison of the evolution of the ratio of total tumour masses to tumour invasion area over macro-micro stages 1 – 100 for the macro-dynamics case* (10) *for various fusion probabilities* p_0*. (i)* $p_0 = 0.25$*, when* $b_s = b_i$ *and* $\delta_s = \delta_i$*; (ii)* $p_0 = 0.75$ *when* $b_s = b_i$ *and* $\delta_s = \delta_i$*. (iii)* $p_0 = 0.25$ *when* $b_s = 1.5b_i$ *and* $\delta_s = \frac{\delta_i}{5}$*; (iv)* $p_0 = 0.75$ *when* $b_s = 1.5b_i$ *and* $\delta_s = \frac{\delta_i}{5}$*.*

better predictions on possible treatment outcomes.

Acknowledgements

The first author would like to acknowledge the support received from the Saudi Arabian Cultural Bureau in the UK on behalf of Umm Al Qura University.

Appendix A. Sensitivity analysis for ECM Initial Conditions

In Figure A.19, we explore the sensitivity of heterogeneity within the ECM initial conditions on the overall viral therapy. We consider three cases for the ECM initial condition, which range from completely homogeneous ECM to certain level of spatial inhomogeneities in the ECM. These are given mathematically through

$$u(x,0) = \frac{1}{2} + \gamma \frac{(0.3sin(4\pi \|x\|_2) + sin(4\pi \|(4,0) - x\|_2))}{2}.$$

where the parameter γ controls the heterogeneity level. Finally, in this numerical experiment we use the baseline parameters set 1 alongside the one-dose virus initial condition presented in 3(c). Figure A.19 shows the outcome of this sensitivity exploration, and we observe there that as ECM heterogeneity increases the tumour evolution moves away from the compact growth exhibited in the homogeneous case, leading to a more complicated tumour morphology.

References

[1] L. Seymour, K. Fisher, Oncolytic viruses: finally delivering, British Journal of Cancer 114 (2016) 357–361.

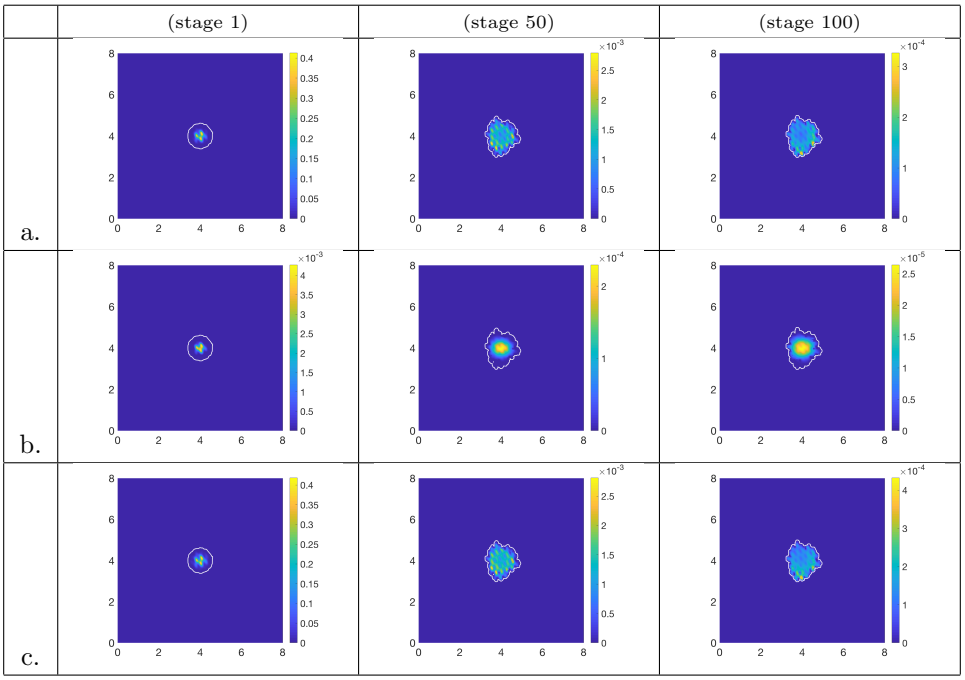

Figure 15: *Multi-scale simulation results for macro-dynamics syncytia system* (10) *at three macro-micro stages (1,50 and 100) for the improved treatment scenario corresponding to the parameter values listed in Table 3, showing: a. infected cancer cells density; b. syncytia cancer cells density and c. total cancer cells density.*

[2] H. Zeh, S. Downs-Canner, J. McCart, Z. Guo, U. Rao, L. Ramalingam, S. Thorne, H. Jones, P. Kalinski, E. Wieckowski, M. O'Malley, M. Daneshmand, K. Hu, J. Bell, T. Hwang, A. Moon, C. Breitbach, D. Kirn, D. Bartlett, First-in-man study of western reserve strain oncolytic vaccinia virus: safety, system spread, and anti tumour activity, Molecular Therapy 23 (1) (2015) 2020–214.

[3] M. Vähä-Koskela, A. Hinkkanen, Tumour restriction to oncolytic virus, Biomedicine 2 (2014) 163–194.

[4] A. Marchini, E. Scott, J. Rommelaere, Overcoming barriers in oncolytic virotherapy, Viruses 8 (9) (2016) 1–22.

[5] S. Meerani, Y. Yao, Oncolytic viruses in cancer therapy, European Journal of Scientific Research 40 (1) (2010) 156–171.

[6] H. Kauman, F. Kohlhapp, A. Zloza, Oncolytic viruses: a new class of immunotherapy drugs, Nature Reviews 14 (2015) 642–662.

[7] T. Krabbe, J. Altomonte, Fusogenic viruses in oncolytic immunotherapy, Cancers 10 (2018) 216.

[8] O. Ebert, K. Shinozaki, C. Kournioti, M.-S. Park, A. García-Sastre, S. L. C. Woo, Syncytia induction enhances the oncolytic potential of vesicular stomatitis virus in virotherapy for cancer, Cancer Research 64 (9) (2004) 3265–3270. doi:10.1158/0008-5472.CAN-03-3753.

[9] A. Sylwester, D. Wessels, S. Anderson, R. Warren, D. Shutt, R. Kennedy, D. Soll, HIV-induced syncytia of a T cell line form single giant pseudopods and are motile, Journal of Cell Science 106 (3) (1993) 941–953.

[10] C. Ayala-Breton, L. Russell, S. Russell, K.-W. Peng, Faster replication and higher expression levels of viral glycoproteins give vesicular stomatitis virus/measles virus hybrid VSV-FH a growth advantage over measles virus, J. Virology 88 (2014) 8332–8339.

[11] H. Higuchi, S. Bronk, A. Bateman, K. Harrington, R. Vile, G. Gores, Viral fusogenic membrane glycoprotein expression causes syncytia formation with bioenergetic cell death: implications for gene therapy, Cancer Research 60 (2000) 6396–6402.

[12] A. Compton, O. Schwartz, They might be giants: does syncytium formation sink or spread HIV infection?, PLoS Pathog. 13 (2) (2017) e1006099.

[13] M. Biesecker, J.-H. Kimn, H. Lu, D. Dinglic, Ž. Bajzer, Optimization of virotherapy for cancer, Bulletin of Mathematical Biology 72 (2009) 469–489.

[14] Z. Bajzer, T. Carr, K. Josić, S. Russell, D. Dingli, Modelling of cancer virotherapy with recombinant measles viruses, Theor. Biol. 252 (2008) 109–122.

[15] A. E.-A. laaroussi, M. E. hia, M. Rachik, E. Benlahmar, Z. Rachik, Analysis of a mathematical model for treatment of cancer with oncolytic virotherapy, Applied Mathematical Sciences 8 (19) (2014) 929–940.

[16] D. Dingli, C. Offord, R. Myers, K.-W. Peng, T. Carr, K. Josić, S. Russell, Z. Bajzer, Dynamics of multiple myeloma tumour therapy with a recombinant measles virus, Cancer Gene Therapy 16 (2009) 873–882.

[17] K. Jacobsen, S. S. Pilyugin, Analysis of a mathematical model for tumor therapy with a fusogenic oncolytic virus, Mathematical Biosciences 270 (2015) 169–182.

[18] D. Berg, C. Offord, I. Kemler, M. Ennis, L. Chang, G. Paulik, Z. Bajzer, C. Neuhauser, D. Dingli, *In vitro* and *in silico* multidimensional modelling of oncolytic tumour virotherapy dynamics, PLoS Comput. Biol. 15 (3) (2019) e1006773.

[19] L. R. Paiva, C. Binny, S. C. Ferreira, M. L. Martins, A multiscale mathematical model for oncolytic virotherapy, Cancer Research 69 (3) (2009) 1205–1211.

[20] T. Alzahrani, R. Eftimie, D. Trucu, Multiscale modelling of cancer response to oncolytic viral therapy, Mathematical Biosciences 310 (2019) 76–95. doi:10.1016/j.mbs.2018.12.018.

[21] D. Trucu, P. Lin, M. A. J. Chaplain, Y. Wang, A multiscale moving boundary model arising in cancer invasion, Multiscale Model. Simul. 11 (1) (2013) 309–335.

[22] L. Peng, D. Trucu, P. Lin, A. Thompson, M. A. J. Chaplain, A multiscale mathematical model of tumour invasive growth, Bulletin of Mathematical Biology 79 (3) (2017) 389–429.

[23] R. J. Petrie, A. D. Doyle, K. M. Yamada, Random versus directionally persistent cell migration, Nature Reviews Molecular Cell Biology 10 (8) (2009) 538–549. doi:10.1038/nrm2729.

[24] M. C. Weiger, V. Vedham, C. H. Stuelten, K. Shou, M. Herrera,

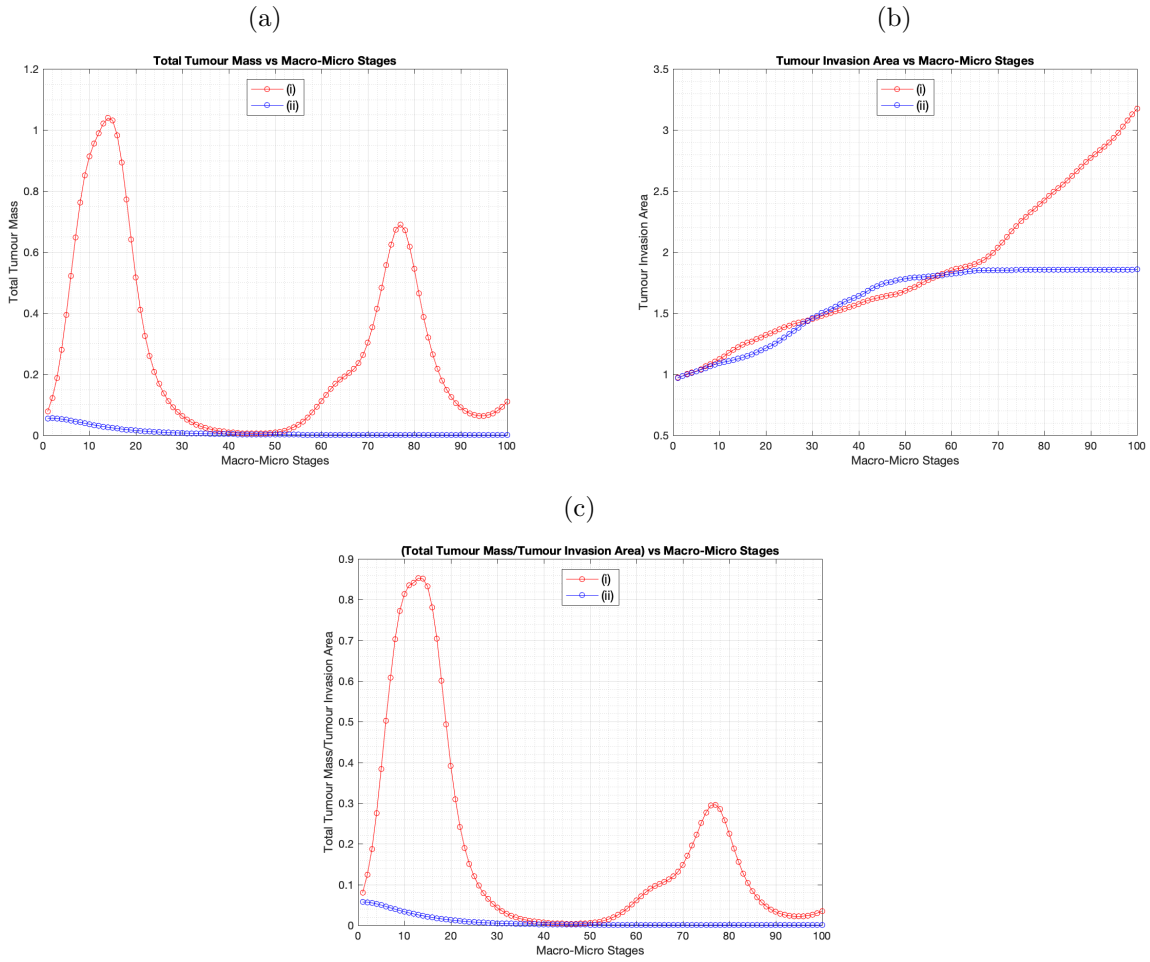

Figure 16: *(a) Comparison of total tumour masses evolution over macro-micro stages 1 – 100 for the macro-dynamics case* (10). *(b) Comparison of tumour invasion area over macro-micro stages 1 – 100 for the macro-dynamics case* (10). *(c) Comparison of the evolution of the ratio of total tumour masses to tumour invasion area over macro-micro stages 1 – 100 for the macro-dynamics case* (10). *(i) baseline parameter values as listed in Table 1; (ii) parameter values for improved anti-tumour therapy as listed in Table 3.*

M. Sato, W. Losert, C. A. Parent, Real-time motion analysis reveals cell directionality as an indicator of breast cancer progression, PLOS ONE 8 (3) (2013) 1–12. doi:10.1371/journal.pone.0058859.

[25] S. Huda, B. Weigelin, K. Wolf, K. V. Tretiakov, K. Polev, G. Wilk, M. Iwasa, F. S. Emami, J. W. Narojczyk, M. Banaszak, S. Soh, D. Pilans, A. Vahid, M. Makurath, P. Friedl, G. G. Borisy, K. Kandere-Grzybowska, B. A. Grzybowski, Lévy-like movement patterns of metastatic cancer cells revealed in microfabricated systems and implicated in vivo, Nature communications 9 (1) (2018) 4539–4539. doi:10.1038/s41467-018-06563-w.

[26] P.-H. Wu, A. Giri, S. X. Sun, D. Wirtz, Three-dimensional cell migration does not follow a random walk, Proceedings of the National Academy of Sciences 111 (11) (2014) 3949–3954. doi:10.1073/pnas.1318967111.

[27] D. W. Stroock, S. S. Varadhan, Multidimensional Diffusion Processes, Springer, Heidelberg, 1997.

[28] A. Anderson, M. Chaplain, E. Newman, R. Steele, A. Thompson, Mathematical modelling of tumour invasion and metastasis, J. Theorl. Medic. 2 (2000) 129–154.

[29] A. K. Laird, Dynamics of tumour growth, British Journal of Cancer 13 (3) (1964) 490–502. doi:10.1038/bjc.1964.55.

[30] A. K. Laird, Dynamics of tumour growth: Comparison of growth rates and extrapolation of growth curve to one cell, British Journal of Cancer 19 (2) (1965) 278–291. doi:10.1038/bjc.1965.32.

[31] K. M. C. Tjorve, E. Tjorve, The use of gompertz models in growth analyses, and new gompertz-model approach: An addition to the unified-richards family, PLOS ONE 12 (6) (2017) 1–17.

[32] D. Hanahan, R. A. Weinberg, The hallmarks of cancer, Cell 100 (2000) 57–70.

[33] R. A. Weinberg, The Biology of Cancer, Garland Science, New York, 2006.

[34] D. Hanahan, R. A. Weinberg, The hallmarks of cancer: The next generation, Cell 144 (2011) 646–674.

[35] L. Venkatraman, S.-M. Chia, B. C. Narmada, J. K. White, S. S. Bhowmick, C. F. D. Jr., P. T. So, L. Tucker-Kellogg, H. Yu, Plasmin triggers a switch-like decrease in thrombospondin-dependent activation of tgf-1, Biophysical Journal 103 (5) (2012) 1060 – 1068.

[36] P. A. Andreasen, R. Egelund, H. H. Petersen, The plasminogen activation system in tumor growth, invasion, and metastasis, Cell Mol Life Sci 57 (1) (2000) 25–40. doi:10.1007/s000180050497.

[37] P. A. Andreasen, L. Kjøller, L. Christensen, M. J. Duffy, The urokinase-type plasminogen activator system in cancer metas-

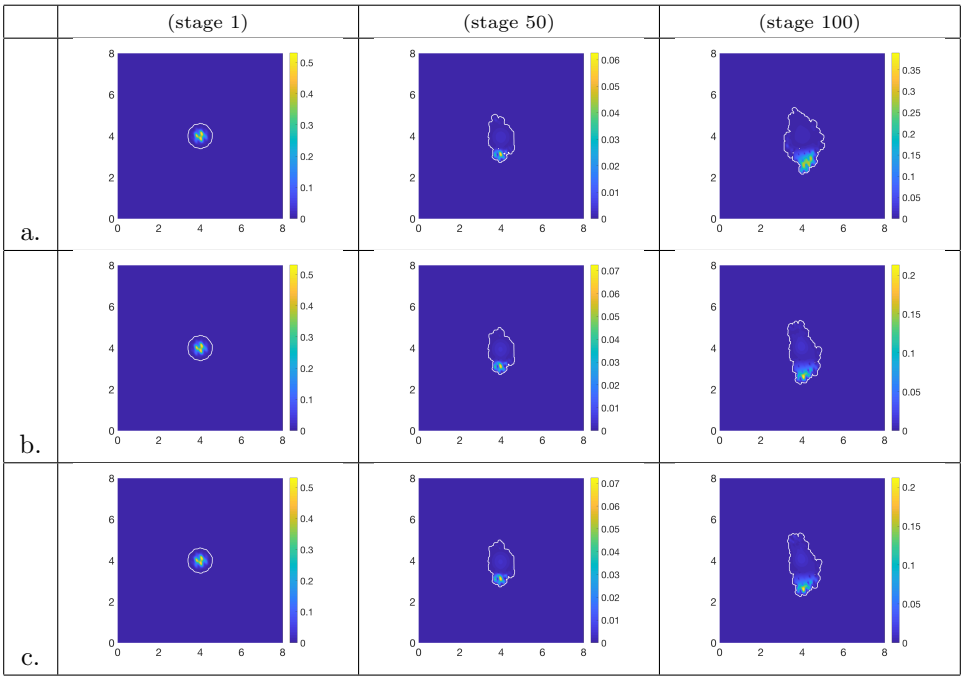

Figure 17: *Multi-scale simulation results for macro-dynamics systems* (10) *(panels (a)),* (17)+(18) *(panels (b)), and* (17)+(19) *(panels (c)), for the baseline parameter values from Table 1. All figures show the total tumour distribution at three macro-micro stages: 1, 50 and 100.*

tasis: a review, Int J Cancer 72 (2) (1997) 1–22.

[38] Y. Bai, P. Hui, X. Du, X. Su, Updates to the antitumour mechanism of oncolytic virus, Thoracic Cancer (2019) 1–5.

[39] B. Hoffner, G. Iodice, E. Gasal, Administration and handling of talimogene laherparepvec: an intralesional oncolytic immunotherapy for melanoma, Oncology Nursing Forum 43 (2) (2016) 219–226.

[40] V. Seery, Intralesional therapy, Clinical Journal of Oncology Nursing 21 (4) (2017) 76–86.

[41] B. I. Camara, H. Mokrani, E. Afenya, Mathematical modelling of glioma therapy using oncolytic viruses, Mathematical Biosciences and Engineering 10 (3) (2013) 565–578.

[42] K.-W. Peng, C. J. TenEyck, E. Galanis, K. R. Kalli, L. C. Hartmann, S. J. Russell, Intraperitoneal therapy of ovarian cancer using an engineered measles virus, Cancer Research 62 (16) (2002) 4656–4662.

[43] F. Herschke, S. Plumet, T. Duhen, O. Azocar, J. Druelle, D. Laine, T. WIld, C. Rabourdin-Combe, D. Gerlier, H. Valentin, Cell-cell fusion induced by measles virus amplifies the type-I interferon response, J. Virol. 81 (23) (2007) 12859–12871.

[44] G. Caravagna, A. d'Onofrio, P. Milazzo, R. Barbuti, Tumour suppression by immune system through stochastic oscillations, Journal of Theoretical Biology 265 (3) (2010) 336 – 345. doi:10.1016/j.jtbi.2010.05.013.

[45] A. d'Onofrio, On the interaction between the immune system and an exponentially replicating pathogen, Mathematical Biosciences & Engineering 7 (3) (2010) 579–602.

[46] A. d'Onofrio, "noisy oncology": Some caveats in using gaussian noise in mathematical models of chemotherapy, in: R. J. Hosking, E. Venturino (Eds.), Aspects of Mathematical Modelling, Mathematics and Biosciences in Interaction, Birkhäuser Verlag AG, Basel, Switzerland, 2008, pp. 229–234.

[47] A. d'Onofrio, Bounded Noises in Physics, Biology, and Engineering, Modeling and Simulation in Science, Engineering and Technology, Birkhauser, 2013. doi:10.1007/978-1-4614-7385-5.

[48] I. Kemler, M. Ennis, C. Neuhauser, D. Dingli, *In Vivo* imaging of oncolytic measles virus propagation with single-cell resolution, Molecular Therapy: Oncolytics 12 (2019) 68–78.

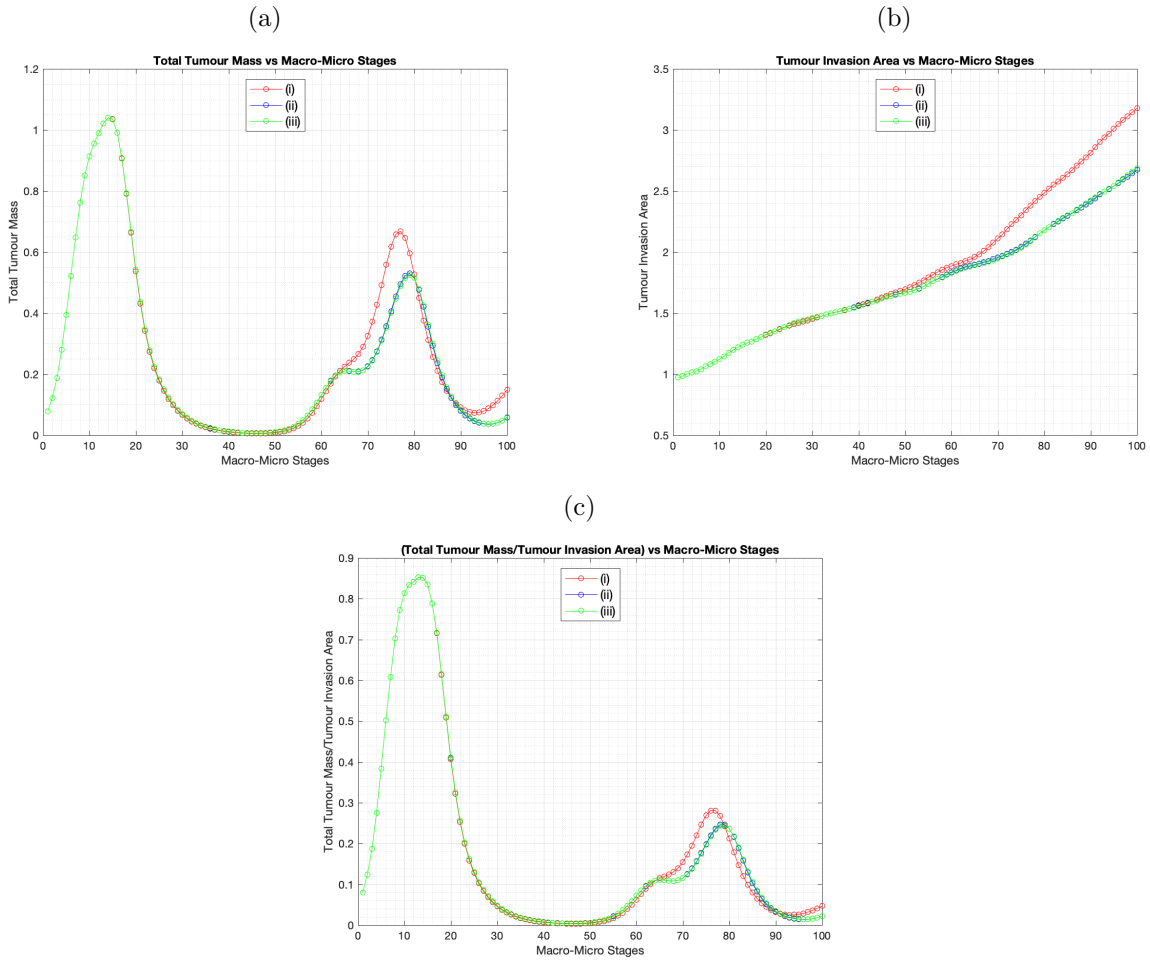

Figure 18: *Comparison between the dynamics of the baseline model* (10) *(red curve labeled (i)) and the generalised model* (17) *(blue curve labeled (ii) for sub-case* (18)*, and green curve labeled (iii) for sub-case* (19)*). (a) The evolution of total tumour mass (uninfected+infected+syncytia cells) over macro-micro stages 1 – 100. (b) The evolution of tumour invasion area over macro-micro stages 1 – 100. (c) The evolution of the ratio of total tumour masses to tumour invasion area over macro-micro stages 1 – 100 for the macro-dynamics case* (17)*. All simulations have been performed using the baseline parameter values from Table 1.*

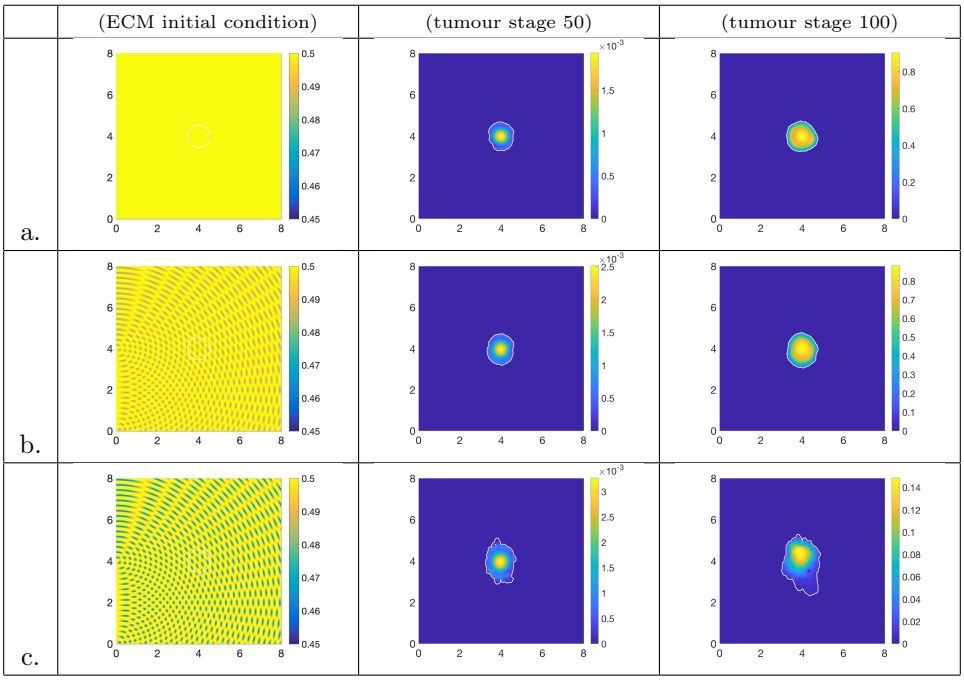

Figure A.19: *Multi-scale simulation involving macro-dynamics* (10) *and three cases of ECM initial conditions, that correspond to the following three levels of the heterogeneity parameter* γ*, namely: a.* $\gamma = 0$*; b.* $\gamma = 0.0625$*; c.* $\gamma = 0.125$*. Left column shows the initial ECM distribution, while middle and right columns show the total tumour distribution at stages (50 and 100).*